GUOHUA LIU

# Synthesis and Applications of Free-standing TiO$_2$ Nanotube Membranes

## Thesis submitted for the degree of Philosophiae Doctor

Department of Micro and Nano Systems Technology

Faculty of Technology and Maritime Sciences

Vestfold University College

2013

VESTFOLD UNIVERSITY COLLEGE

# Declaration

I certify that except where due acknowledgement has been made, the work is that of the author alone; the work has not been submitted previously, in whole or in part to qualify for any other academic award; the content of the thesis is the result of work which has been carried out since the official commencement date of the approved research program; any editorial work, paid or unpaid, carried out by a third party is acknowledged; and, ethics procedures and guidelines have been followed.

*Guohua Liu, Horten*

January 28, 2013

# Abstract

Nanostructured $TiO_2$ nanotubes (TNTs) have great application potential in optoelectronic devices due to large effective light harvesting surface area and wide band gap. Anodization of Ti is a simple way to prepare well-ordered nanostructured $TiO_2$ in the form of vertically oriented TNTs. Compared with dense nanoparticles, TNTs facilitate charge transport along the tube direction while maintaining a high effective surface area, and thus suitable for a variety of applications such as sensors, water splitting, photovoltaic devices, $CO_2$ conversion, supercapacitors etc.

In order to form a well-ordered tubular structure with controlled morphology, a balance between oxidation and field-assisted dissolution has to be maintained by adjusting electrolyte concentration, temperature, anodic duration, ramp rate and the applied potential. However, the nature of TNTs attached to an opaque Ti foil and with a closed bottom limits their feasibility for use in extensive applications. Therefore, built upon suitable fabrication approaches that enable free-standing TNT membranes as well as the investigation of their photoconductive properties so that create environmental friendly alternative energy sources are the motivations of this work.

This Ph.D. work focuses on the challenging issues: i) improve the tune quality of highly ordered TNTs by reproducible manner. ii) Investigate pioneered technologies to prepare the free-standing TNT membrane as well as mechanism behind the detachment process. iii) Explore the photoconductive property of the TNTs. Following progresses have been made towards the target.

**Article I** provided an overview of all technologies to prepare free-standing TNT membranes. The developments of structural optimization techniques of the detached membrane are described from electrochemistry point of view. The application status for solar cells, water splitting, hydrogen sensors, supercapacitors, $CO_2$ reduction and photocatalysis are highlighted.

**Article II** developed a simple process to fabricate flat and mechanically robust free-standing amorphous TNT membranes. Rinsing the as-prepared TNT membranes by pure ethanol and reducing the rate of ethanol evaporation are key steps to prepare a large scale, flat surface membranes. **Article III** performed a voltage-dependent investigation for the detachment process of free-standing crystalline TNT membrane. The membrane

detached at low voltage preserves its nanotube morphology and the bottom of tubes are closed, while through-hole membrane with fast detachment can be observed at a high detachment voltage.

**Article IV** reported controllable fabrication of free-standing crystallized TNT membranes and study their photoconductive properties by optoelectronic technique. The membrane exhibits a sensitive spectral response to the UV light. These photoresponse origins from internal gain induced by desorption of oxygen molecules from the nanotube surfaces and reduction of the barrier at neighboring tubes under UV illumination.

**Article V** compared the UV light sensitivity between the small diameter nanotubes ~ 20nm and the conventional 140nm diameter TNTs. The small diameter nanotube device enhances the UV photoresponsivity and leads to a larger increase of photocurrent. We attribute this improvement to the modulation of hole carrier density as a result of field effects from the diameter-dependent population of the surface-trapped electrons.

**Article VI** investigated the effects of applied potential, anodized duration and post-treatment on the growth and morphology of the anodic TNTs. **Article VII** carried out a series of electrochemical anodization experiments to understand the formation mechanism and to increase control over the morphology of free-standing TNT membranes.

**Article VIII** aims to review current knowledge of photocatalytic conversion of $CO_2$ towards solar fuels over $TiO_2$. The basic principle of photocatalytic synthesis is described, and then engineering design of the $TiO_2$ photocatalysts are emphasized with respect to reaction parameters. The links between photocatalytic properties of nanostructured $TiO_2$ and $CO_2$ conversion by using solar energy are addressed. In addition, rationally orienting the nanostructured $TiO_2$ in chemical reactors for the $CO_2$ conversion and prospects are highlighted for further development.

**Key words**: Anodization, $TiO_2$ nanotubes, Free-standing membranes, Photoconductivity, Solar fuels.

# Preface

This thesis is submitted in candidacy for the Ph.D. degree from Vestfold University College (VUC), Norway. It is based on the work carried out at Department of Micro and Nano Systems Technology, VUC-IMST from January 2010 to December 2012. Financial support was provided by the KD program (08665) at the VUC, Oslofjord Fund and NorFab consortium in Norway.

I would like to thank my first supervisor Professor Kaiying Wang for his guidance, encouragement and support during my PhD candidature. I am especially grateful for his tireless assistance on my experiments and papers. Special thanks to my second supervisor associate Professor Nils Hoivik, for his enlightening ideas and discussions to my work. Many thanks to master student Wenran Gu, Waqas Ahmad, Qiong Chen and Ying Zhao for their continuing friendship.

I am also grateful to the VUC staffs, IMST laboratory members as well as my research friends. Appreciations go to the following people for their technical assistance and guidance: Prof. Einar Halvorsen and Knut Aasmundtveit for their invaluable input of knowledge; Zekija Ramic and Ragnar Dohansen for help of the experimental set up; Tormod Vinsand for help with SEM; Vishnukanthan Venkatachalapathy for help of XRD; Xiaoming Wang for help of TEM.

Last but not least, my deepest appreciation and sincere gratitude are extended to my parents and relatives for their unconditional love, understanding and support accompany along my PhD journey. None of this would be possible without their love and concerns.

*Guohua Liu, Horten*

January 28, 2013

# List of articles

**The thesis is based on the following five papers:**

I. <u>Guohua Liu</u>, Kaiying Wang, Nils Hoivik and Henrik Jakobsen, Progress on free-standing and flow-through TiO₂ nanotube membranes, *Solar Energy Materials and Solar Cells*, 98 (2012) 24-38. (Top 25 Hottest Articles in 2012 full year)
Contribution: Material collection, Draft writing

II. <u>Guohua Liu</u>, Kaiying Wang, Nils Hoivik and Henrik Jakobsen, Reducing solvent evaporation rates for the detachment of anodic TiO₂ nanotubular membranes, *MRS Online Proceedings Library*, 2012, Volume 1442.
Contribution: Experiment, Manuscript preparation

III. <u>Guohua Liu</u>, Nils Hoivik, Kaiying Wang and Henrik Jakobsen, A voltage-dependent investigation on detachment process for free-standing crystalline TiO₂ nanotube Membranes, *Journal of Materials Science*, 46(2011)7931-7935.
Contribution: Experiment, Data analysis and interpretation

IV. <u>Guohua Liu</u>, Nils Hoivik, Xiaoming Wang, Shushen Lu, Kaiying Wang and Henrik Jakobsen, Photoconductive, free-standing crystallized TiO₂ nanotube membranes, *Electrochimica Acta*, 93 (2013) 80-86.
Contribution: Conception, Experiment, Data analysis

V. <u>Guohua Liu</u>, Nils Hoivik and Kaiying Wang, Small diameter TiO₂ nanotubes with enhanced photoresponsivity, *Electrochemistry Communications*, 28 (2013) 107-110.
Contribution: Conception, Experiment

**Additional contributions:**

VI. <u>Guohua Liu</u>, Kaiying Wang, Nils Hoivik and Henrik Jakobsen, Growth and morphology of highly ordered TiO₂ nanotube arrays via electrochemical anodization, *ECS Transactions*, 41 (2012) 19-27.
Contribution: Experiment, Data analysis

VII. <u>Guohua Liu</u>, Nils Hoivik, Kaiying Wang and Henrik Jakobsen, Free-standing TiO₂ nanotube membranes from electrochemical anodization, *IEEE, NANO* No.127 (2011) 1011-1015, August 15-19, Portland, Oregon, USA.
Contribution: Experiment, Draft writing

VIII. <u>Guohua Liu</u>, Nils Hoivik, Kaiying Wang and Henrik Jakobsen, Engineering TiO₂ nanomaterials for CO₂ conversion/solar fuels, *Solar Energy Materials and Solar Cells*, 105 (2012) 53-68. (Top 25 Hottest Articles from July to December 2012)
Contribution: Material collection, Draft writing

**Publications not enclosed in the thesis:**

IX. Waqas Ahmad, <u>Guohua Liu</u>, Nils Hoivik, Kaiying Wang, Ultraviolet Photodetector Translated from Crystalline TiO₂ Nanotube Arrays, *Proceedings of the 3rd International Conference on Nanotechnology: Fundamentals and Applications*, Montreal, Quebec, Canada, 7-9 August 2012, Paper No. 300
Contribution: Conception

X. Qiong Cheng, Waqas Ahmad, <u>Guohua Liu</u> and Kaiying Wang, Structural Evolution of Amorphous Thin Films of Titanium Dioxide, *IEEE, NANO* No.306 (2011) 1589-1601, August 15-19, Portland, Oregon, USA.
Contribution: Writing improvement

# Contents

# Abbreviations

| | |
|---|---|
| SEM | *Scanning electron microscopy* |
| EDX | *Electron dispersion or energy dispersive X-ray spectroscopy* |
| TEM | *Transmission electron microscopy* |
| XRD | *X-ray diffraction pattern* |
| SAED | *Selected area electron diffraction pattern* |
| UV | *Ultraviolet* |
| DSSCs | *Dye-sensitied solar cells* |
| FTO | *Fluorine doped Tin oxide* |
| E | *Applied electric field or Young's modulus* |
| $\sigma$ | *Stress* |
| T | *Temperature* |
| U | *Potential at the electrode [V]* |
| I | *Photocurrent* |
| i | *Ionic current* |
| $X_{barrier}$ | *Thickness of the barrier layer* |
| ICP | *Inductively coupled plasma etching* |
| wt.% | *Weight %* |
| vol.% | *Volume %* |
| A | *Area* |
| D | *Nanotube diameter* |
| L | *Length of nanotube* |
| $\delta$ | *Wall thichness* |
| CB | *Conduction band* |
| VB | *Valence band* |
| $e^-$ | *Electron* |
| $h^+$ | *Hole* |
| $\mu$ | *Carrier mobility* |
| n | *Carrier* |
| $\Delta\sigma$ | *Photoconductivity* |
| Pt | *Platinum* |
| Ti | *Titanium* |
| $TiO_2$ | *Titanium dioxide, titania* |
| TNT(s) | *TiO₂ nanotube (arrays)* |
| $F^-$ | *Fluorine ion* |
| DI | *Deionized* |

# 1 Introduction

## 1.1 Background

$TiO_2$ is a wide band gap semiconductor, which has been broadly studied in water splitting [1, 2], dye sensitized solar cells (DSSCs) [3, 4], photocatalysis [5, 6] and sensors [7, 8] on the basis of its chemical stability and unique functional properties. Compared with dense nanoparticles, $TiO_2$ nanotubes (TNTs) are suggested to be superior in chemical and optoelectronic performance due to its one-dimensional channel for carrier transportation, in which the recombination of $e^-/h^+$ is expected to be reduced [4, 9]. Of a variety of $TiO_2$ synthesis strategies, particular interest has been given to the anodic oxidized growth of TNT layers on Ti foil, as it leads to an array of closely packed vertically aligned tubes [9, 10]. Growth of highly ordered TNTs with a length of a few hundred nanometres has been first reported using electrochemical anodization of Ti foil in aqueous hydrofluoric acid solution [11]. Very high aspect-ratio TNTs grown up to hundreds of micrometres in length were also obtained through anodization of Ti in organic electrolytes [12]. However, the nature of TNT arrays attached to an opaque Ti substrate and with a closed bottom has restricted their feasibility for use in extensive applications [10, 13]. Recent studies imply that free-standing TNT membranes have more interesting performance than that of the TNT layer on Ti foils [13]. Key features of free-standing TNT membranes lie on their absence of barrier layer at the tube bottom, direct electrons transferring, stability to mechanical vibrations and they can be integrated or transferred on any foreign substrates, which making them ideal structures for a spectrum of applications in energy and environmental areas.

## 1.2 Application status

- Integration of TNT membranes on the transparent and conductive substrate is an efficient strategy. The best photovoltaic performance of DSSCs based on TNT membranes reached 8.80%, which is higher than that of a $TiO_2$ nanoparticle

electrode (7.58%) because of the reduced electron combination and efficient light-harvesting efficiency [14, 15].

- The free-standing TNT membrane with open-ends shows an increased efficiency in water splitting. A maximum conversion efficiency of 0.70% was obtained with the open-ended TNT membrane/FTO, which was much higher than the 0.22% efficiency obtained by the closed-ended TNT membrane/FTO or 0.36% by the TiO$_2$ particle/FTO electrode [16].

- The TNT-membrane sensor is more sensitive than that of the membrane adhered on Ti substrates. The variation of the resistance of a 25 µm thick free-standing TNT membrane reaches 25 times when it is exposed to 1000 ppm hydrogen for 1800s, in contrast to 11 times for the films on Ti substrate. The blocking layer that formed between the TNT and the Ti substrate after annealing should be the main reason account for the difference in sensitivity. Besides, the response of the free-standing membrane is much quicker than that with Ti substrate due to which provides flow-through channels that accelerate the diffusion of H$_2$ into the nanotubes [17].

- A cocatalyst loaded TNT membrane for high rate photocatalytic conversion of CO$_2$ and water vapor into hydrocarbon fuels is demonstrated. With this assembly coupled with an outdoor global AM 1.5 sunlight, hydrocarbon production rate of 111 ppm cm$^{-2}$ h$^{-1}$ was obtained when the nanotube arrays are loaded with both Cu and Pt nanoparticles. This rate of CO$_2$ to hydrocarbon production is at least 20 times higher than previous published reports. The high CO$_2$ adsorption capacity was ascribed to the synergetic effect of the high surface area tubular morphology and the mixed-valence nanoparticles [18, 19].

- A free-standing and flow-through TNT membrane has been designed for a novel reactor. Via bleaching methylene blue solution under UV irradiation, the membrane exhibits higher photocatalytic activity than the one with closed-ended. The decomposition rate was determined by the diffusion rate, complete pollutant removal was observed by one flow-through cycle through the membrane [12, 20].

- A novel type of artificial K$^+$-gated ion channels based on titania nanotube membrane loaded with Au nanoparticles and G-rich DNA composite structure was developed. This fabricated permselective membrane using K$^+$ as a trigger may set light to the field of biosensing, drug-release, ion exchange membrane and so on [21].

## 1.3  Aims and Tasks

From the literature survey, we concluded that TNT membranes demonstrate remarkable behaviors that warrant further study, underlying the large number of researchers working in this field. The exciton dissociation and carrier transportation are the two key taches restricting the performance of optoelectronics. To obtain better performance, increasing the active area of materials in devices and restricting the transport direction of carriers to make sure of their directional transportation are straightforward strategies. In this thesis, we follow the point of tailoring materials at nanoscale toward the challenges, focus on synthesizing free-standing crystalline TNT membranes from Ti foils for developing cost-effective and high performance optoelectronics. Apart from meeting both requirements perfectly, an added value of this work is that it provides physical insight into the photoconductivity of TNT network and presents an important advance toward the integration of nanomaterials for optoelectronic applications.

## 1.4  Outline of thesis

The thesis is organized based on the published and submitted articles. The first chapter "Introduction" presents the motivations fueled me to conduct the investigations and the dissertation outline. In Chapter 2 "Summary of the articles", five articles are collected. All the articles are briefly introduced and discussed. Each article represents a stage of my work. These articles are textured in a systematic way to show the progress of the research step by step. The full-length articles are enclosed at the end of thesis. In Chapter 3 "Conclusions", contribution of this work to science is summarized.

# 2 Summary of the articles

In this section, five articles are selected to highlight the research content during Ph.D. studies. The research consists of three packages: (1) an overview of all technologies to prepare TNT membranes in Article I; (2) Experimental fabrication of TNT membranes in Article II and Article III; (3) Photoconductive study of TNTs in Article IV and Article V; The collected articles are organized in terms of the research stage, rather than the publication date. The full-length articles are enclosed at the end of thesis.

## 2.1 Literature review (Article I)

The as-prepared TNT membrane adhered on opaque titanium foil restricts their feasibility for many applications, such as tube filling, molecular separations and catalysis, where flow-through of the nanotubes arrays is required [13, 20, 22]. The physical properties and morphology of an open-end membrane depends on the specified process parameters [23-25]. Normally, large residual stresses are introduced by specific processes. Highly stressed membranes accumulate large amounts of strain energy. When the strain energy release rate exceeds the interfacial toughness of the membrane, delamination ensues and peels off from the surface [26]. Residual stress in thin membranes comprises two main components: (i) thermal stress due to mismatching of coefficients of thermal expansion of film and substrate materials and (ii) intrinsic stress due to all other factors, like chemical reactions, ion diffusion, lattice mismatch or different material properties etc. If the membrane is prepared at temperature of $T$, and $T_o$ is room temperature, $E_m$ is Young's modulus, $v_m$ is Poisson's ratio of the membrane material, then assuming $E$ and $v$ to be temperature independent, this stress is written as [26]

$$\sigma_{th} = \left\{ \frac{E_m}{(1-\nu_m)} \right\} \int_{T_o}^{T} \left( \alpha_m - \alpha_{substrate} \right) dT \tag{1}$$

where $\alpha_m$ and $\alpha_{substrate}$ are the coefficients of thermal expansion of the membrane and substrate, respectively. Values of elastic constants and thermal expansion coefficients of Ti / TiO₂ are $\alpha_{Ti} = (9.41\sim10.03)\times10^{-6}$/ °C, $\alpha_{TiO2} = 8.7\times10^{-6}$/ °C, $\nu_{TiO2} = 0.28$, $E_{TiO2} = 282.76$ GPa. But the real mechanism behind the detachment process is complicated and not well understood as yet. Herein, typical methods to detach the TiO₂ nanotube membrane and make it capable of flow-through are discussed in this section. The related techniques and mechanism are sketched as in Fig.1.

### 2.1.1 Mechanical delamination (Fig.1A: Solvent evaporation / Ultrasonic vibration / Peeling-off by tape)

*Solvent evaporation induced delamination*

Methanol [12, 27, 28] and DI water [29] are commonly used rinsing liquids and solvents. A possible detachment mechanism of solvent evaporation induced free-standing membrane is understood as multilayer delamination (Fig.1, method A). Although the nanotube membrane surface is rinsed and kept in an organic bath after electrochemical anodization, a small amount of $H^+$ and $F^-$ still remain in the regions between adjacent nanotubes. A slow etching caused by the remaining $H^+$ and $F^-$ ions led to structural defects. Moreover, rinsing the sample with liquid methanol (surface tension ~22.1dynes/cm at room temperature), the liquid diffused into the interpore regions and wet the defect surface [28]. Subsequently, slow evaporation in the defect areas induces the delamination of the barrier layer driven by the surface tension.

After rinsing the prepared sample with solvents, a mild ultrasonic in methanol is often adopted to get rid of nanofibrous debris on the surface. The cleaned membrane is then left to dry in air with the anodized surface facing up. A brownish colored membrane is then separated from the Ti foil during the evaporation of the methanol. A gentle mechanical bending of anodized Ti foil facilitates complete detachment of the membrane [28]. The membrane dimension is flat in wet conditions, dramatically cracking, fracturing, and curling into many small pieces during drying in atmosphere. It is believed that a combination of both surface tension forces and strain gradients account for this curling. To overcome the curling, super critical point drying was proposed to prepare flat, mechanically robust membranes [12].
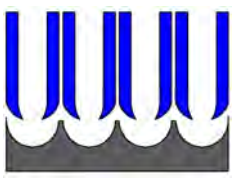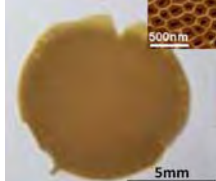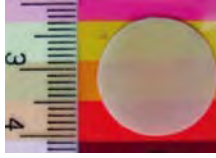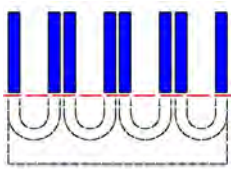
| Method | Schematic | Mechanism | Example | Comments |
|---|---|---|---|---|
| **A**<br><br>Mechanical delamination | | Mechanical splitting | | A facile and safe method, need further step to open end |
| **B**<br><br>Physicalparameter regulation | | Electrochemical extraction | | A simple and green method, open end directly |
| **C**<br><br>Chemical separation | | Chemical dissolution or assisted separation | | Robust method to prepare free-standing membranes |
| **D**<br><br>Selective dissolution or ICP etching | | Selective dissolution or physical etching | | Reliable method to prepare flexible nanotubular flow-through membranes |

**Fig. 1.** Detachment and open bottom methods for the membrane (A) Mechanical delamination, the example from [14], (B) Physical parameter regulation, the example from [23], (C) Chemical separation, the example from [37], (D) Selective dissolution or ICP etching, and the example from [46].

*Ultrasonic vibration induced delamination*

Ultrasonic vibration induced detachment is based on nonlinear effects developed in a liquid, which causes cavitation, erodes surface, and create microjets from pulsating cavities. During the ultrasonic vibration, collapsing cavities or cumulative microjets produce high pressure pulses, which induce stress on the solid surface [17]. The primary stress between the interface of barrier and bottom of amorphous TiO₂ nanotubes is due to the mismatch of crystalline structures. The responses of the barrier and bottom layer to the oscillation in ultrasonic bath are different, which result in secondary stress at the interface. Besides, the additives of H₂O increase the solution acidity and accelerate the dissolution of TiO₂ at the interface of metal/oxide, causing the formation of defect zone. Increasing the defect zone region reduces the threshold for the interface to be split off.

Several parameters have been discussed on the stress occurrence during ultrasonication, such as frequency, temperature, static pressure, vapor pressure, and surface tension. The surface tension and vapor pressure are two major factors, which are defined by the ratio of water to organic solvent (i.e. ethanol) in ultrasonic bath. The surface tension of water

and ethanol is $72.75 \times 10^{-3}$ and $22.32 \times 10^{-3}$ N/m, while the vapor pressure is 17.5 and 44.6 mm Hg at 293 K respectively [17]. Thus, adding a certain amount of water in ethanol increases the solution acidity as well as enhances the surface tension. Applying ultrasonic vibration in a solution of water and ethanol with 1:4 volume ratios and followed by drying in atmosphere, a large-area and non-collapsing free-standing thin $TiO_2$ nanotube membrane was detached from Ti substrate [17]. In even lower water concentration, ultrasonic agitation in 95% ethanol solution for several minutes, a thicker $TiO_2$ nanotube membrane was detached due to the low acidity, and the bottom ends of the membrane were opened in a 5 wt% $NH_4F$-1M $H_2SO_4$ solution for 15 min [30, 31].

*Direct peeling-off by tape*

Peeling-off by Scotch tape is a straightforward method to separate inorganic $TiO_2$ membrane from Ti foils by mechanical force [32]. However, the detached membrane are easily curled or broken since the flexibility of the tape. Another better solution for fabricating self-supporting membranes is to detach the oxide films with an adhesive polymer, followed by soaking it in organic solvent to remove the polymer. Alternatively, the transfer printing technique developed by Rogers and co-workers was applied to detach the nanotube membrane [33].

### 2.1.2 Physical parameter regulation (Fig. 1B: Voltage, Temperature, Electrolyte composition)

*Voltage control*

Decreasing and increasing voltage at the end of the anodization reduce adhesion of $TiO_2$ nanotube layer on Ti substrate, and simultaneously open up the bottom ends [23, 25, 34-36]. This method is attributed to local acidification and gas evolution produced by voltage transition. Through the voltage transition at the end of anodization, the bottom end morphology was tailored by tuning the magnitude and duration of the anodized voltage and the barrier layer at the bottom becomes fragile. Thus, both the breaking away of the $TiO_2$ nanotubes from the Ti foil and the opening of their bottoms can be easily achieved. This method is simple and offers a number of advantages in comparison to chemical etching by HF.

As an example of this technique, a constant voltage of 100 V for 2-3 h in $NH_4F$/ethylene glycol electrolyte was carried out by using computer controlled power supply. At the end of the process, the voltage was decreased by software or manually adjusted

potential to 10 V, over 0.5-1 minute. Following the fabricated TiO$_2$ nanotube layer was detached by sonication in a methanol bath, and membranes with through-hole morphology were observed [23]. In our recent experiment, the immobilized membranes with ordered TiO$_2$ nanotube arrays are prepared in ethylene glycol electrolyte under 60V/24 h first, then after annealing at 500 $^{\circ}$C for 2 h, followed by another anodized at 20, 60, 100 V for 60, 30, 10 minutes, respectively. All of the membranes were successfully detached from the substrate by taking advantage of the different mechanical stress of the two anodic layers [25]. On the contrary of decreasing the final step voltage, free-standing and flow-through TiO$_2$ nanotube layers were also observed by raising the voltage from 60 V to 80-180 V at the end of process [34-36].

*Temperature control*

A thermal treatment has been applied for as-prepared TNT membrane on titanium foils to assist membrane detachment [22, 25, 37]. The process is described as three steps [37]. First, the Ti substrate is electrochemically pre-anodized. Then the pre-anodized TiO$_2$ layer is peeled off by intense sonication in deionized water to expose the electrochemically patterned Ti substrate. The patterned substrate Ti is then anodized once more, and the new oxide layer is heat-treated at a temperature range of 200-700 $^{\circ}$C. The initial two electrochemical anodization steps were carried out at 10 $^{\circ}$C in electrolyte while the third one at an elevated temperature 30-50 $^{\circ}$C. The free-standing membranes are completely detached by the third step.

This method utilized the different mechanical stability and etching selectivity between upper and lower tube layers [22, 38]. After thermal treatment, anatase crystals formed on the upper layer show high resistance to chemical etching. While the bottom tube layer formed by third-step anodization has an amorphous structure. Therefore, the crystallized TiO$_2$ layers can easily be mechanically peeled off by taking the advantage of the different material properties between the anodic layers. The elevated bath temperature is crucial for the membranes separating. The high temperature at the third step gives rise to low viscosity and high current density for the electrolyte, which leads to enhanced chemical etching ability. Local chemical dissolution is expected to be fast for newly formed TiO$_2$ nanotubes, which has less dense walls at the interface and weak interconnection.

*Electrolyte composition control*

By regulating the composition and concentration of electrolytes, detached $TiO_2$ nanotube array membranes were achieved directly due to etching contrast between the oxide layers and the substrate [39, 40]. As sodium molybdate (0.1M) was added in ethylene glycol solution containing 2% water and 0.5% ammonium fluoride, free-standing transparent TNT membranes were synthesized. The membrane was amorphous $TiO_2$ with thickness equal to 10 µm. After a hydrothermal treatment at 120 $^O$C, amorphous $TiO_2$ nanotubes were transformed to anatase structure while the integrity structure of the membranes was maintained [40].

### 2.1.3  Chemical separation (Fig. 1C: Chemical dissolution/Chemical assisted separation)

*Chemical dissolution*

A dense and free-standing membrane consisting of both-side-open $TiO_2$ nanotubes was detached from metallic Ti substrate by chemical dissolution process [20]. In this process, a high aspect ratio $TiO_2$ nanotubular layer was first prepared on Ti substrate. Then the specimen was immersed into a mixture of $Br_2$ and dry methanol for 12h in $N_2$ atmosphere. This created a free-standing nanotube membrane floating in the etching solution. After being rinsed with methanol and DI water, the layers were placed (closed tube side down) above an open bottle containing HF 48% for preferential etching of the tube ends. Finally, the sample is rinsed with DI water again. The final membrane allows direct, size-selective, flow-through photocatalytic reactions with high efficiency. However, this fabrication method takes long process time and used a toxic bromine-containing methanol solution.

*Chemical assisted separation*

The solutions $H_2O_2$, HCl, HF and $HgCl_2$ have been employed for chemical assisted separation of $TiO_2$ nanotubes membrane from Ti substrates [16, 37, 41-45]. The as-prepared nanotube array membranes and Ti substrate were immersed in 33 wt% $H_2O_2$ solution for tens of second, following which the entire $TiO_2$ nanotube membrane was lifted off from the Ti substrate with a closed ends [16, 41]. Then, oxalic acid was used to remove the tube ends. During this wet-chemical etching, a thin layer of hot-melt adhesive was used as a protective layer to cover on the opened top of the nanotube arrays for retaining its tubular structure first. The free-standing array membrane was

then immersed in 0.5% oxalic acid solution at 40 °C for a certain time. Titanium oxide located at the interface of the tube and the bottom ends was etched by oxalic acid to form a yellow titanium oxalate complex. After the bottom ends fell off and the open pores appear, the thin protective layer was separated by soaking the adhesive in acetone solution [16].

An alternative method is that amorphous TiO₂ nanotube layer is crystallized by high-temperature annealing at 330-500 °C in oxygen ambient. Then a thin underlayer of amorphous nanotube layer is grown underneath the annealed TiO₂ nanotube layer by a secondary anodization step. Next, the amorphous lower-layer is selectively dissolved by a treatment in 5% H₂O₂ solution for 12 hours. The crystallized titania nanotube membrane present an excellent anticorrosion ability in the solution and was separated from the Ti substrate without any cracking [37].

Etching bottom layer in 0.1 M aqueous HCl solution for 1 hour is another option to prepare free-standing membranes [43, 44]. The free-standing membrane was manipulated with tweezers and transferred onto fluorine doped tin oxide (FTO) glass substrate. Besides, free-standing TiO₂ nanotube membrane was peeled off by soaking the films in a saturated HgCl₂ solution for several hours, leaving self-supporting membrane and the titanium substrate [45].

### 2.1.4 Selective dissolution or ICP etching (Fig. 1D: Selective dissolution/ ICP etching)

*Selective dissolution*

This technique consists of anodizing a pre-formed metallic double layer Ti/Al and followed by a wet etching technique. The electrochemical parameters are adjusted to allow for nanotube formation in metallic Ti layer. Once the thin Ti layer is fully anodized, it continues to etch into the underlying aluminum layer. The anodized double layer (Ti/Al) membranes are then immersed in ethanol and dried in air. Last, the aluminum and formed alumina pores are selectively removed in an acidic etchant. Albu et al. have demonstrate the fabrication of a large-scale, flexible and well electrically connected nanotubular flow-through TiO₂ nanotube membranes by taking this technique [46]. This strategy allowed large-scale membranes to be reliably fabricated for the first time. A prior photolithographic definition of pore-array squares shows much advantage to provide rupture-free structures, mechanical flexibility, and high conductivity via the

remaining Ti metallic frameworks. An alternative approach to prepare $TiO_2$ nanotube arrays with through-hole morphology by anodizing a thermally evaporated Ti/Au bilayer film also have been demonstrated [47].

*ICP etching*

Inductively coupled plasma etching uses reactive plasma to micro machine semiconductor materials. High-energy ions from the plasma attack the materials and the plasma-assisted reaction produce volatile compounds which are pumped out from the ICP system. Thus, the barrier layer at the bottom of the titania nanotube arrays could be removed by ICP etching to get flow-through titania nanotube arrays [21, 48]. For instance, the flow rate of plasma etching parameters were He 20 sccm, $Cl_2$ 10 sccm, $BCl_3$ 40 sccm with a base pressure equal to 0.8-0.9 Pa. After plasma etching for 10 min, the bottom ends of the titania nanotube arrays were completely opened [21]. Compared to previous attempts, these approaches are scaled up to large areas and eliminate the critical bottom opening steps, and compatible with standard MEMS technology.

### 2.1.5 Advance in photoconductive studies of TNTs

The characteristics of photocarrier dynamics in semiconductors are the basis of the operation of photodetectors, photodiodes, and solar cells, and they typically include photogeneration of electron-hole pairs, their efficient transport, and collection as the output signal. The photoconductivity in a semiconductor can be defined as $\Delta\sigma_{photo} = e\mu\Delta n$, where $e$ is the electronic charge, $\mu$ is the carrier mobility and $\Delta n$ is the carrier concentration [49-51]. Nanostructured materials are attractive for photon detection because of their large active surface area and potential integration with conventional electronics [49, 50]. In a semiconductor nanowire/ nanotube, the electron-irradiation-carrier dynamics just like the photo-carrier dynamics could be strongly affected by carrier trapping and/or scattering at the surface localized energy states over the bulk energy states, particularly due to the large surface-to-volume ratio. Earlier examples of semiconductor nanowire (Ge, ZnO) photodetectors indicate that the response process is strongly influenced by temporal and spatial charge separation and carrier multiplication within one dimensional confinement [51, 52]. The photoconductivity is size-dependent and inversely proportional to the nanowire diameter, as shown in Fig. 2.
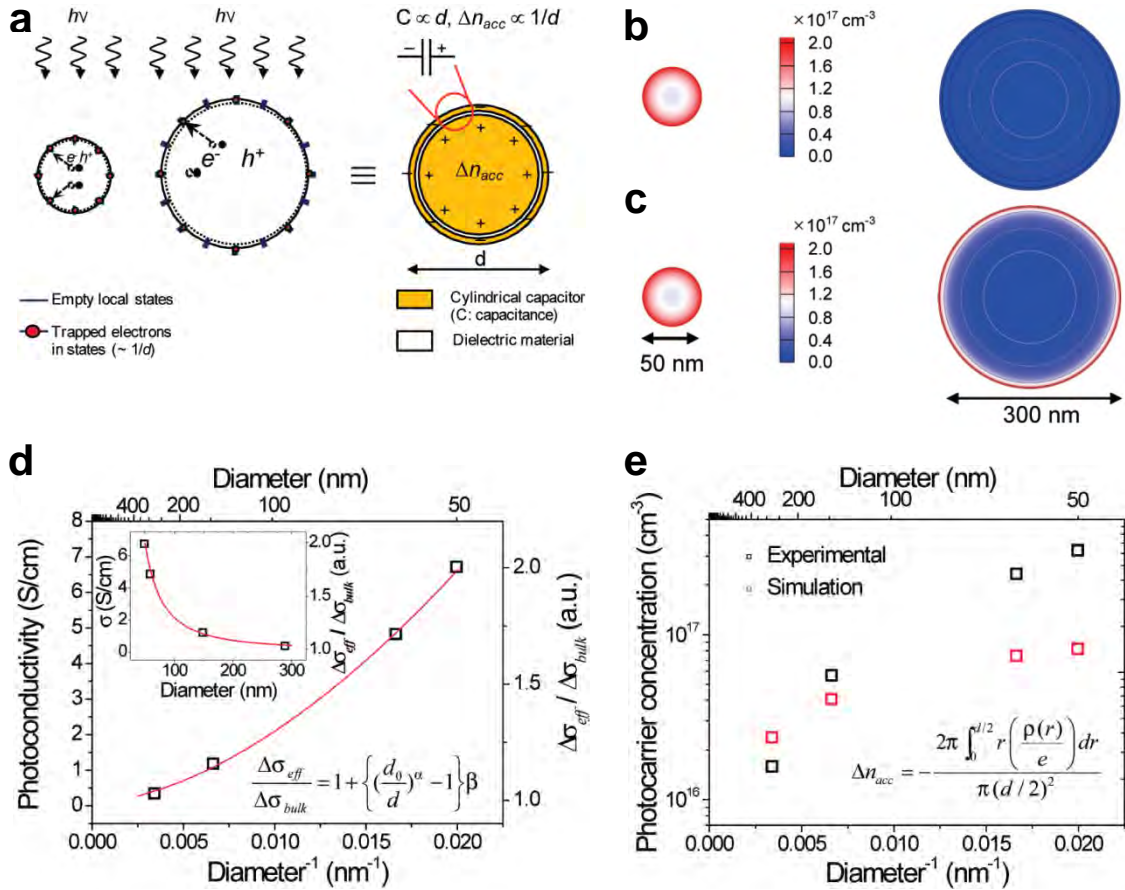
**Fig. 2.** Diameter-dependent photoconduction (a) illustration of the photocarrier generation by the low photon flux and subsequent electron surface trap and hole accumulation at the nanowire (NW) cross sections with different diameters, which is similar to a cylindrical capacitance. (b, c) Two-dimensional simulation of the induced hole concentrations (filled colors) for 50 and 300 nm thick Ge NW cross sections. (b) The induced hole concentrations at lower photon flux as in the case of (a). (c) The induced hole concentrations in the case of full saturation of surface states upon the higher photon flux. Contours in each NW cross-section image represent the equipotential line (gray). (d) Diameter dependence of the photoconductivity. (e) Diameter dependence of the photocarrier concentration when the gain is maximal [51].

TiO₂ nanostructures such as nanotubes, nanowires/rods are one of the main groups for the fundamental research and development of real-world nanoelectronics [4, 8-10]. The distinctive UV absorption ability makes TiO₂ suitable for UV detection against the background of infrared and visible light [8]. The anisotropic geometry of the one-dimensional structure facilitates rapid transport of carrier, which is crucial for optimizing the carrier collection efficiency [53, 54]. Various aspects of TiO₂ photodetectors have been addressed by downsizing from bulk to nanometer in literature. Earlier studies are devoted to understand the dynamics of the transport, trapping and recombination of charge carriers generated in TiO₂ nanoparticle films [55, 56]. However, it is a challenge to extract the intrinsic transport properties from the size effects in dense

nanoparticle films. Subsequent in situ observations of photoconduction properties over the 1D TiO$_2$ nanostructures provide a means of exploring the surface and size effects on the electrical transport phenomena [53, 57-59]. Nevertheless, their manufacturing is complicated and not suitable for large-scale applications. Recent studies are focused on device performances by using TiO$_2$ rods/tubes as building block that leads to a filling/decoration of nanostructures [8, 54, 60, 61]. For such composites, it is difficult to extract details on rod/tube-induced transport properties as that represents a mixture of material behavior. Despite the progress, fundamental questions about the internal electronic structure, the effect of the large surface or small size in comparison to its bulk, and size dependent transport phenomena in TiO$_2$ nanotubes remain scarcely answered up to now.

## 2.2 Fabrication of TiO$_2$ nanotube membranes

### 2.2.1 Amorphous free-standing TNT membranes (Article II)

In this work, we developed a facile procedure for fabricating free of disorder nanostructuress, large-area, flat and mechanically robust TNT membranes. The major highlights of this approach are (i) straightforwardly detaching a large scale TNT membrane from Ti substrate after a single anodization step. (ii) Rinsing the as-anodized film with ethanol effectively avoids the architectural disorder on the membrane surface. (iii) Reducing evaporation rate of the rinsing solvent assures the detachment of a large area, flat surface and free-standing membrane.

*Experiment*

Prior to anodization, Ti foils were cut into required size (~15mm×35mm×0.3mm, 99.8% purity), and degreased by sonicating in acetone, isopropyl alcohol and methanol each for 10 min. Then the Ti sheets were rinsed with DI water and dried in air. The anodization was carried out in a two-electrode system with a platinum foil as a counter electrode and Ti sheet as a working electrode. The distance between cathode and anode was fixed to 3.5cm. Anodization was conducted at a constant voltage of 80V for 24 h at room temperature. Ethylene glycol (99.8 wt%, Sigma-Aldrich) containing 0.5 wt% ammonium fluoride and 0.3 wt% DI water was used as the electrolyte.

The fabrication processes are schematically shown in Fig. 3. A Ti foil (Fig.3a) is anodized to form TNT arrays (Fig. 3b). The as-prepared arrays are rinsed by ethanol and

then covered by a piece of heavy duty cleanroom paper (TX5729) to assure a slow evaporation (Fig.3c). Last these TNT arrays are self-detached from the substrate during evaporation process and result in a flat free-standing TNT membrane (Fig. 3d). As a comparison, another as-anodized sample was rinsed with DI water and drying in the air. Furthermore, the membranes were annealed to obtain the crystalline phases.
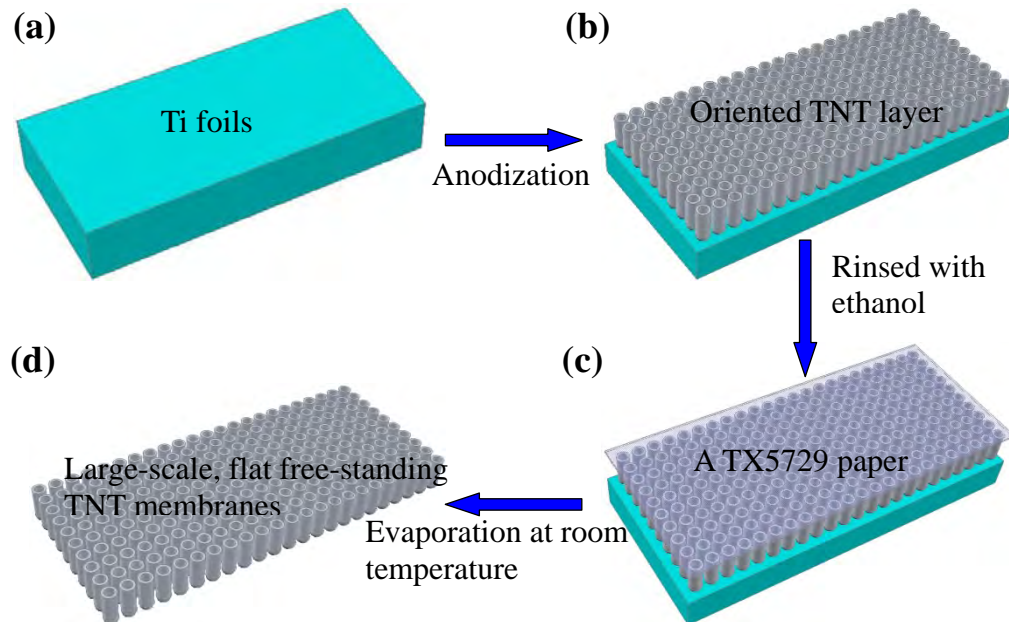


**Fig. 3.** Schematic illustration of the fabrication process

The morphology and the structural quality of membranes were investigated by scanning electron microscope (SEM, Philip EX-30) and transmission electron microscope (TEM, JEM-2010HR). The TNTs were scratched from the sample and dispersed in ethanol, and one drop of the suspension was dropped onto a carbon-coated copper grid for HRTEM and SAED measurements. The crystal structure of membranes was identified by X-ray diffraction (XRD, Bruker AXS D8 Discover) using Cu Kα radiation.

*Discussion*

Fig. 4 (1) and (2) show photographs of the obtained free-standing TNT membranes. The membrane (Fig. 4 (1)) was rinsed by DI water and dried in atmosphere [34], the free-standing TNT layer was detached from Ti substrates during the water evaporation. The surface of the membranes was flat in wet status while they dramatically cracked and curled into small pieces after drying. From the top-view SEM image in Fig. 4(a), it can be seen that both clusters of TNT bundles and microcracks exist in the membrane structure. The disorder nanowires (inset in Fig. 4(a)) were caused by the nanotube lateral deflection resulting from the action of capillary forces between adjacent

nanotubes during evaporative drying. The extents of bundling and crack are supposed to increase with increasing the membrane thickness [62, 63]. Fig. 4b displays the cross-section SEM image of the membrane. The TNT length is about 300 μm. The tube tips are sparse while the bottom parts are closely connected, a combination of both surface tension forces and strain gradients account for the curling [34].

The anodized TNT membrane rinsed with ethanol, and then covered by a piece of heavy duty cleanroom paper to slow down the evaporation rate. After drying and removing the paper, a free of disorder nanostructures, large scale, free-standing and mechanically robust TNT membrane was observed, as shown in Fig. 4(2). The large area detachment of the TNT membrane can be understood through the low drying rate, which induces the tension force between the membrane and metallic substrates to be released uniformly. Although a free-standing TiO$_2$ nanotube membrane was developed based on methanol wetting and subsequent N$_2$ blow-dry technique [64], the N$_2$ air turbulences along the blowing streams might obsess the fragile membranes to reach a large scale. Moreover, ultrasonically cleaning the surface induced unevenly strain and tension forces over the whole membrane and easily crumbled the membrane into small pieces [28]. In contrast, ethanol has a relatively low surface tension and evaporation rate; herein the whole membrane remains an intact and flat surface after drying. It can be seen from the top-view SEM image (Fig. 4c) that the amount of morphological disorder was significantly reduced. The magnified image (inset of Fig. 4c) shows that the TNT arrays remain compact, stand vertically and no destructive changes are observed after peeling from the Ti substrate. The constituted TNTs are of an average diameter of 150 nm and wall thickness of ~15 nm. Fig. 4d shows cross-section SEM image of the membrane, where the TNT length is about 300 μm. The estimated aspect ratio (length/diameter) of the membrane is ~ 2000, which is an important parameter for photoelectrochemical application [10, 28].
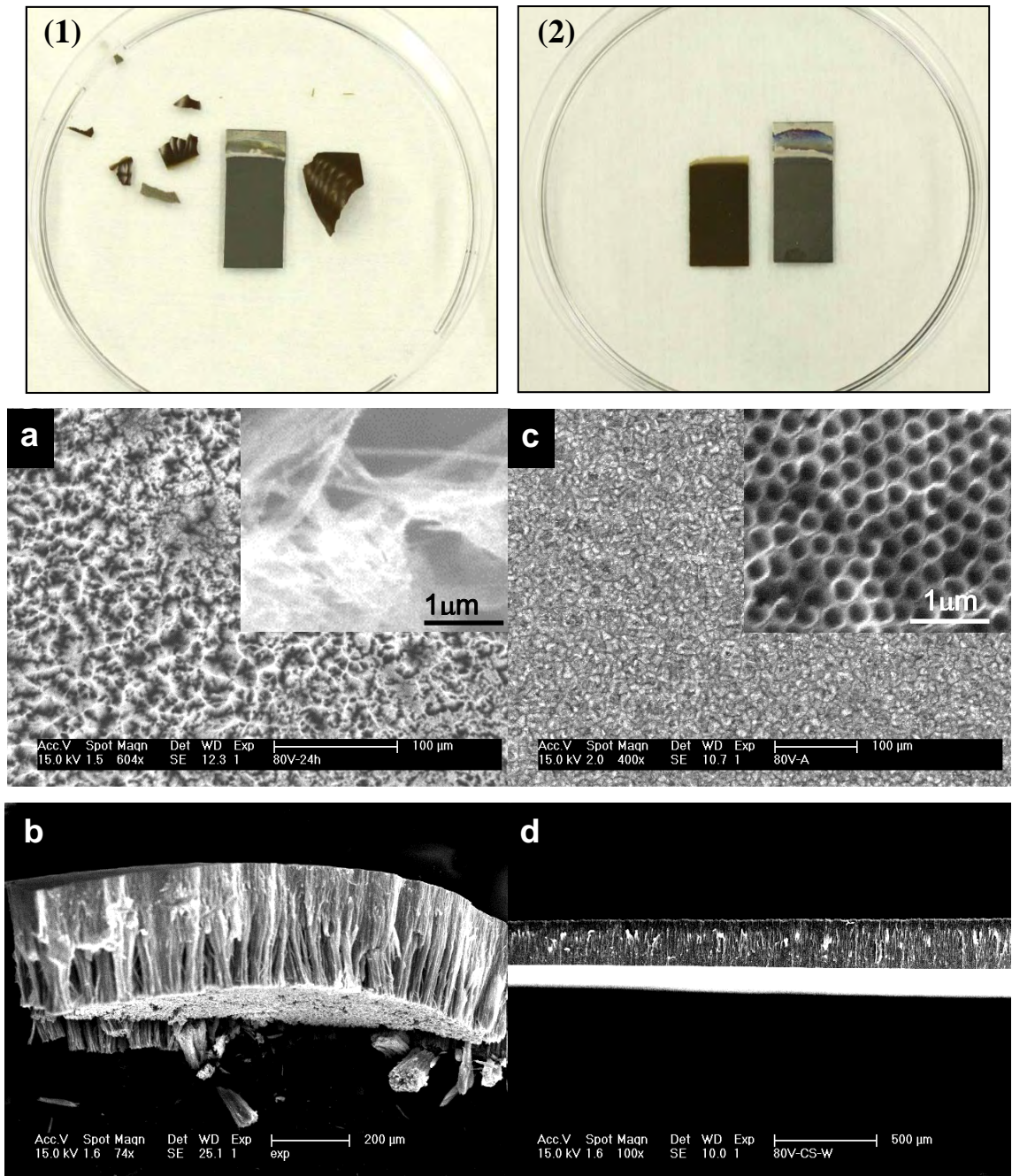
**Fig. 4.** Digital photographs of free-standing TNT membranes rising with (1) DI water or (2) pure ethanol. SEM images of the membranes cleaned with water (a) top-view, (b) cross-section, cleaned with ethanol (c) top-view, (d) cross-section.

Fig.5 presents an angle-view photograph and detailed SEM images (insert) of a large scale, flat, free-standing TNT membrane and the corresponding Ti substrate. The membrane is mechanically robust and can be easily manipulated with tweezers, standing perpendicularly without any bending. The surface SEM image (insert Fig.5a) shows an ordered and compact nanotube array rather than disordered nanowire structure. The cross-section image (Fig. 5b) illustrates that these pores are consisted of densely packed nanotubes. This vertically oriented, close-packed morphology of nanotube arrays go

straightly from the top to bottom of the membrane and provide a direct pathway for electron transport at the nanotube walls. The bottom image of the membrane and the remained footprint on the substrate are presented in Fig. 5c, d, respectively. It can be seen that the membrane bottom consisted of close-packed TNTs with a closed end. The diameter of the end is ~200 nm and a barrier layer existed between the TNTs and the Ti substrate.

Specifically in the barrier layer, the ions migrated through the oxide film and upon arrival at the oxide-metal interface forms a sacrificial soluble oxyfluoride layer. This thin layer consists of various anions ($F^-$, $O^{2-}$, $OH^-$) and metal cations $Ti^{n+}$ combined in many different ways. Prior study indicated that the relatively fast migration of fluoride ions as compared to other ions (such as $O^{2-}$) account for the poor adhesion between the oxide membrane and the underlying substrate [32]. Therefore, the applied voltage is the dominant factor to the growth and the self-detached process of TNT arrays. Generally, low voltage (0-40 V) results in an immobilized TNTs with thin thickness, high voltage (>80 V) and long duration cause over-etching on the surface, leading to disorder nanostructures left on the surface [65-67]. Thus, the membrane fabrications were all conducted in the potential range of 40-80 V [34-42, 68], but few researcher emphasized this critical step. In this study, anodization at 80 V for 24 hours was proved to be balance the material contrast and the growth rate of the TNT tube. As a result, it not only produced the membrane with enough mechanical strength but also led to a facile detachment.
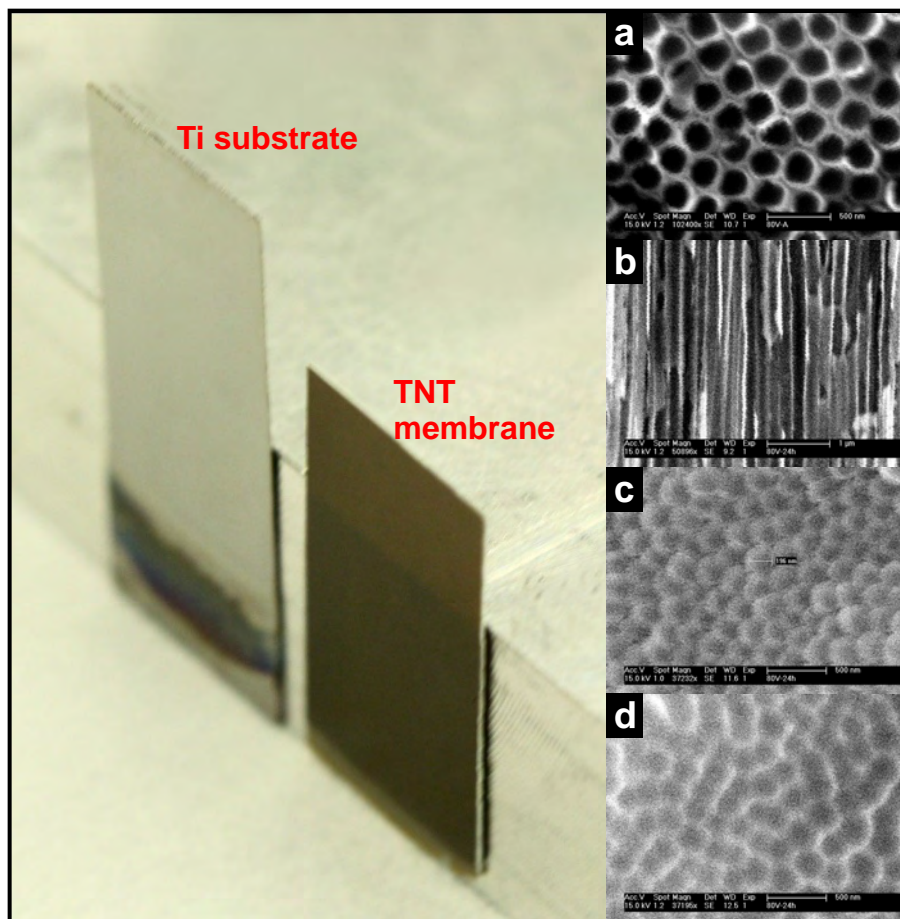
**Fig. 5.** Self-standing TNT membranes (a) top view (b) cross-section (c) bottom view (d) corresponding foot print left on the substrate

The phase of TNT arrays is amorphous after electrochemical anodization. High resolution transmission electron microscope (HRTEM) image (Fig. 6a and c) shows a disorder amorphous characteristic. A large number of localized states in the amorphous structure can act as traps and recombination centers [69-71], which reduce the TNT performance (e.g. photo-catalytic/electronic). To crystallize the titanium dioxide, the TNTs were annealed in air with the temperature ramping at a rate of 2 °C/min and then kept at 500 °C for 2 h. Crystallized and ordered structure of the TNT is immediately apparent after annealing, as shown in Fig. 6b and d. XRD characterization (Fig. 6e) further confirmed that the as-prepared TNT is amorphous and no obvious peaks can be found. On the contrary, the crystallized counterpart shows three strong diffraction peaks. All reflections are indexed (marked by black bar in Fig. 6e-JCPDS file 84-1286), the diffraction peaks at 2θ= 25.5°, 38.1°, 48.3° can be identified to the (101), (004), (200) crystal faces, respectively. The grain diameter estimated from TEM analysis is 80 nm while Scherrer analysis of the X-ray patterns give a value of 82 nm from the (101) diffraction peak.
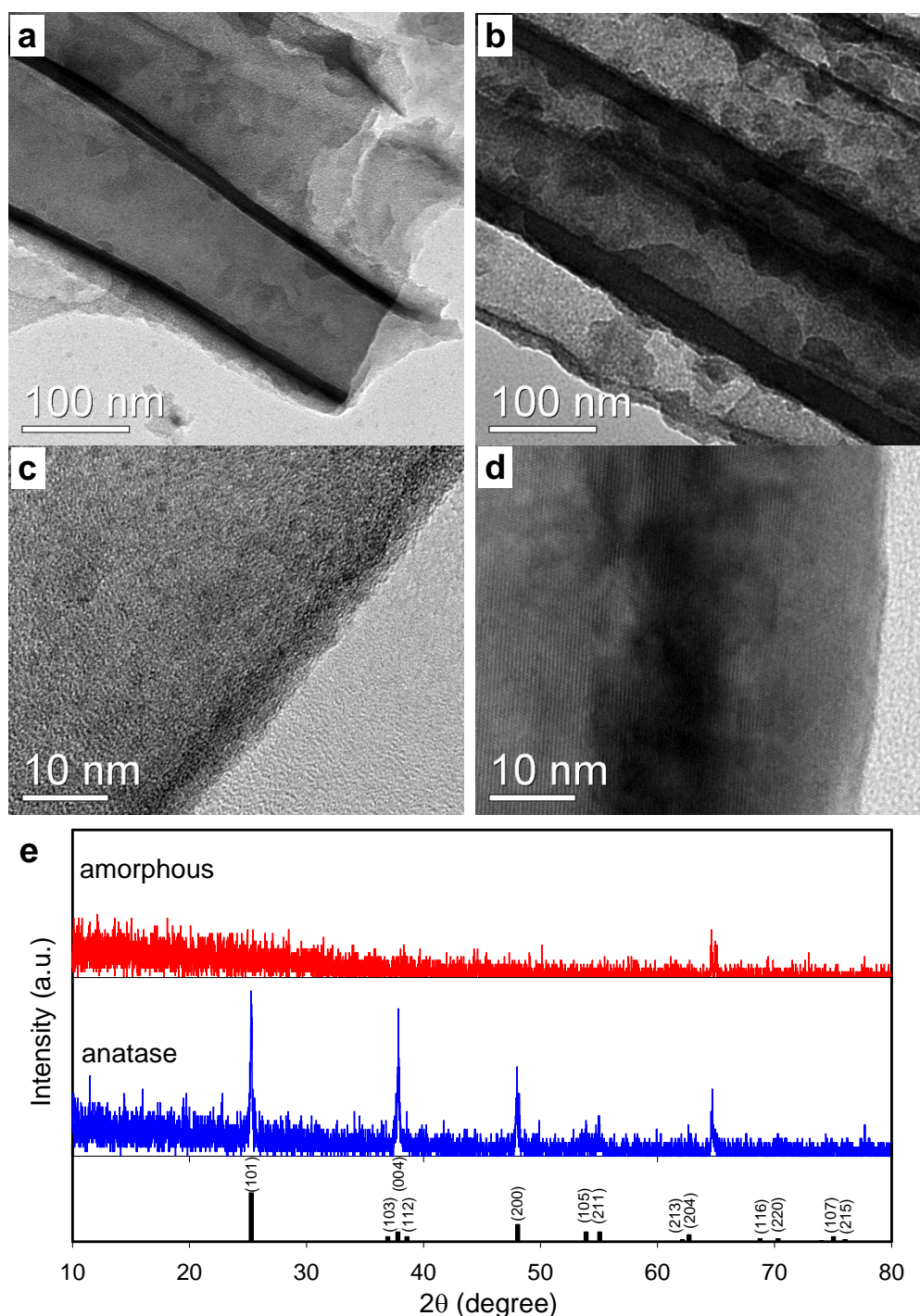
**Fig. 6.** TEM images of the amorphous (a) and anatase TNT (b), (c) and (d) are the selected area electron diffraction (SAED) patterns, (e) XRD patterns of the TNTs

### 2.2.2 Free-standing crystalline TNT membranes (Article III)

In this paper, a handy experimental procedure was proposed to fabricate free-standing crystalline TNT membranes. The concept is outlined in Fig. 7 (1)-(4). The ordered TNT arrays are firstly fabricated under optimized parameters, after an annealing and followed by a second (detachment) anodization step, free-standing crystalline TNT membranes are detached from the substrate without any cracks. Low detachment voltage (20V)

results in closed end membranes, while through-hole membranes are obtained at a high detachment voltage (100V). This method is a reliable technique for fabricating free-standing TNT membranes without the needs for any complicated processes or dangerous chemicals. At the same time, different from previous studies, we have systematically investigated the effects of voltage on the detachment process of free-standing crystalline TNT membranes.

*Experiment*

Ti foils were cut into required size (~15mm×35mm×0.3mm, 99.8% purity, obtained from Baoji Titanium Industry Co., Ltd, China), degreased and cleaned by sonication in acetone, isopropanol and deionized water for 10 min during each step. After drying, the backside of Ti foil was covered by a Scotch tape, rinsed by water and exposed to UV radiation about 10min for cleaning. Then it was put into a polyflon cell with an area of 4 cm$^2$ exposed to the electrolyte. Ethylene glycol with 0.5 wt% ammonium fluoride ($NH_4F$) and 3 vol% water was used as electrolyte. The first anodization was started with growth of ordered TNT arrays on Ti foil under 60V for 24 h, followed by sonic cleaned in ethanol to remove the electrolytes and annealed at 500 $^oC$ for 3 h to crystallize the TNT arrays. Then, the annealed samples were anodized again in the same stock electrolyte with another voltage (e.g. 20, 60, 100 V). After detecting the detachment occurs over time to each case, the samples were picked out and rinsed by ethanol to remove the electrolytes, finally dried in air. The morphology of the TNT membranes was characterized by a Philip EX-30 scanning electron microscope (SEM). X-ray diffraction analysis (Bruker AXS D8 Discover with a normal θ-2θ scan, Cu-Kα radiation) was performed for phase identification.

*Results and discussion*

Fig.7 (a-c) shows the photographs of free-standing crystalline TNT membranes and their substrates with various detachment voltages (second anodization). The membrane geometry was defined by the first anodization (60V/24 h) [45, 72], but the applied voltages in second anodization step were 20, 60 and 100 V respectively, corresponding to the sample a, b and c. It can be seen that the membranes formed with white color, free of cracks and only slightly bending upon air drying. This bending effect may be ascribed to the absence of barrier layer at tube bottom, where compressive stress is exerted.
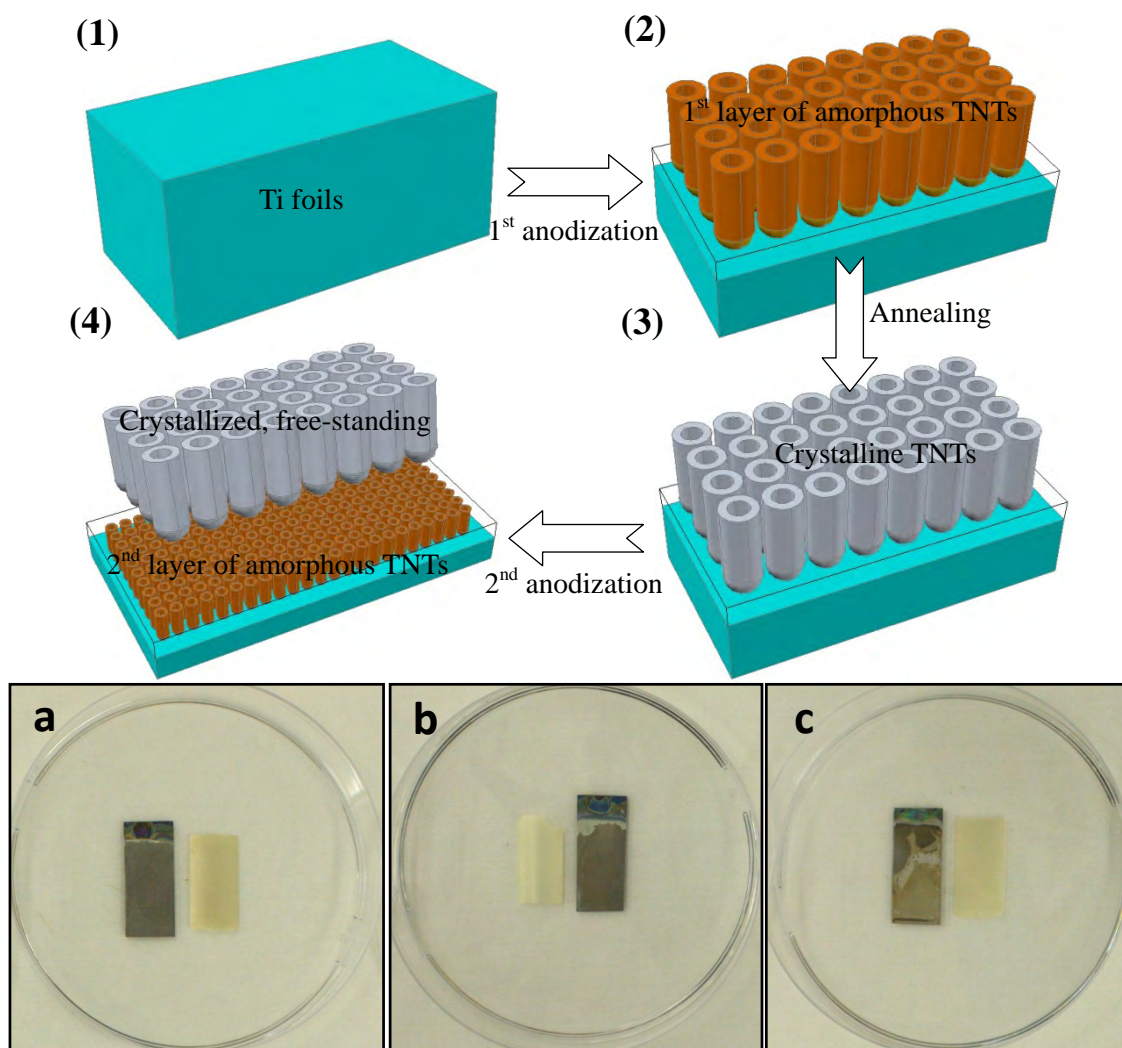
**Fig. 7.** Schematic illustration of the fabrication process for free-standing crystalline TNT membranes (1)~(4) and (a~c) the three resulting samples are firstly anodized at 60V/24h, then annealing at 500 °C/3 h, followed by another anodization at 20V/60 min, 60V/30 min and 100V/10 min, respectively.

Fig. 8 shows the top view, cross section and bottom view SEM images of the above three membranes. From the top view and cross section images in Fig. 8a-c, it can be observed that all membranes (the inserts of Fig. 8 a-c) display a thickness of 18 μm and the average inner diameter of 140 nm, which are not influenced by the second anodization step. This phenomenon indicates that crystallized layer shows high resistance to chemical etching from the electrolyte. Fig.8 d-f shows the surface of Ti substrates after detachment and bottom morphology of the membranes. It can be seen in Fig.8d and its insert that the membrane detached at low voltage (under 20 V for 60 minutes) preserves their tube morphology and the bottom of tubes are closed, and a non-ordered compact oxide layer is present on the bottom of membrane. As shown in Fig. 8e, the nanotube bottom ends are opened partly in 30 minutes with the detachment voltage

equals to 60 V. On the other hand, all bottom ends of the nanotube are homogenously opened at the high detachment voltage (100 V), and the through-hole diameter is about 50 nm as present in the inset of Fig. 8f. Besides, the detachment process at high voltage is faster than that of the low voltage, and it only needs about 10min.

To clarify the detachment mechanism of the free-standing TNT membranes, top-view SEM images of the membranes (Fig. 9a-c) and the images of underlying TNT layer remaining on substrate (Fig. 9d-f) were further analysed. We can see that the tip wall thickness of the TNT on membrane is about 15nm. However, the wall thickness and inner diameters of the underlying tube on substrate are 10, 25, 45nm and 30, 60, 80 nm corresponding to the 20, 60 and 100 detachment voltage, respectively. The interface structures of membranes before detachment might be presumed as the schematic diagrams in Fig. 9. The possible detachment mechanism of the TNT arrays from the substrate can be explained as follow: a TNT layer prepared under a set of parameters leads to a specific geometry, the underneath layer may be initiated at the bottom of a tube [34, 73-76], or in the spaces between the tubes [73]. The crystallized/amorphous oxide interface forms from various anions ($F^-$, $O^{2-}$, $OH^-$) and metal cations $Ti^{n+}$ combined in different ways. The relatively fast migration of fluoride ions as compared to other ions (such as $O^{2-}$) induced a poor adhesion between the layers [32].
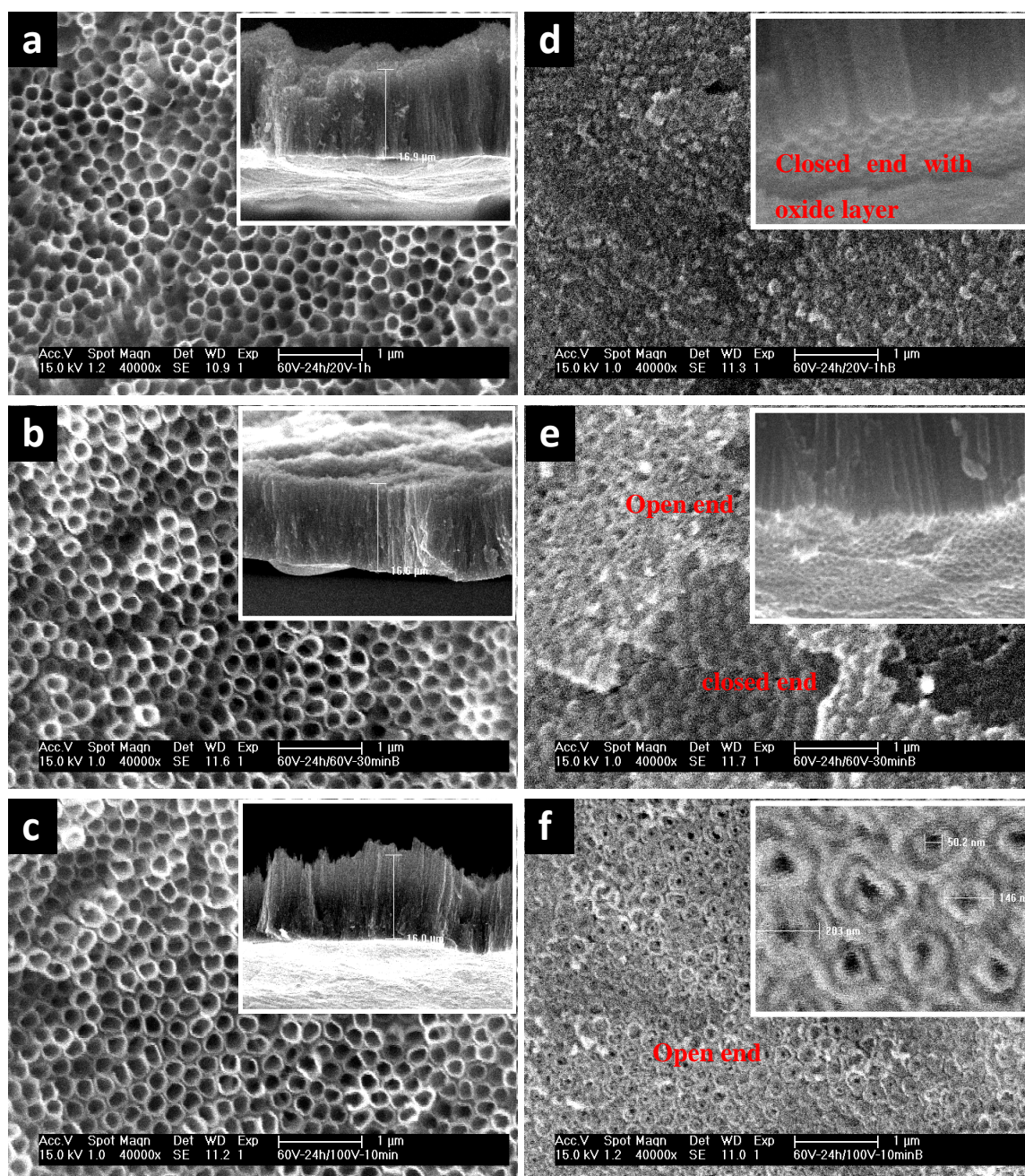
**Fig. 8.** (a-c) Top view, cross-section (inert) and (d-f) bottom view images for the membrane a~c in Fig.7.

Furthermore, different from previous studies, the local acidification and gas evolution produced by transition voltage [34] and mechanical contrast account for the detachment of present study. Therefore, all methods can effectively detach the TNT membrane. But the membrane detachment more likely occurs below the interface (as marked by blue dash-line) at low voltage and above the interface at high voltage due to sharp contrast of material properties and the resulting structure. To the middle voltage (60V), the detachment is random distributed over the interface.
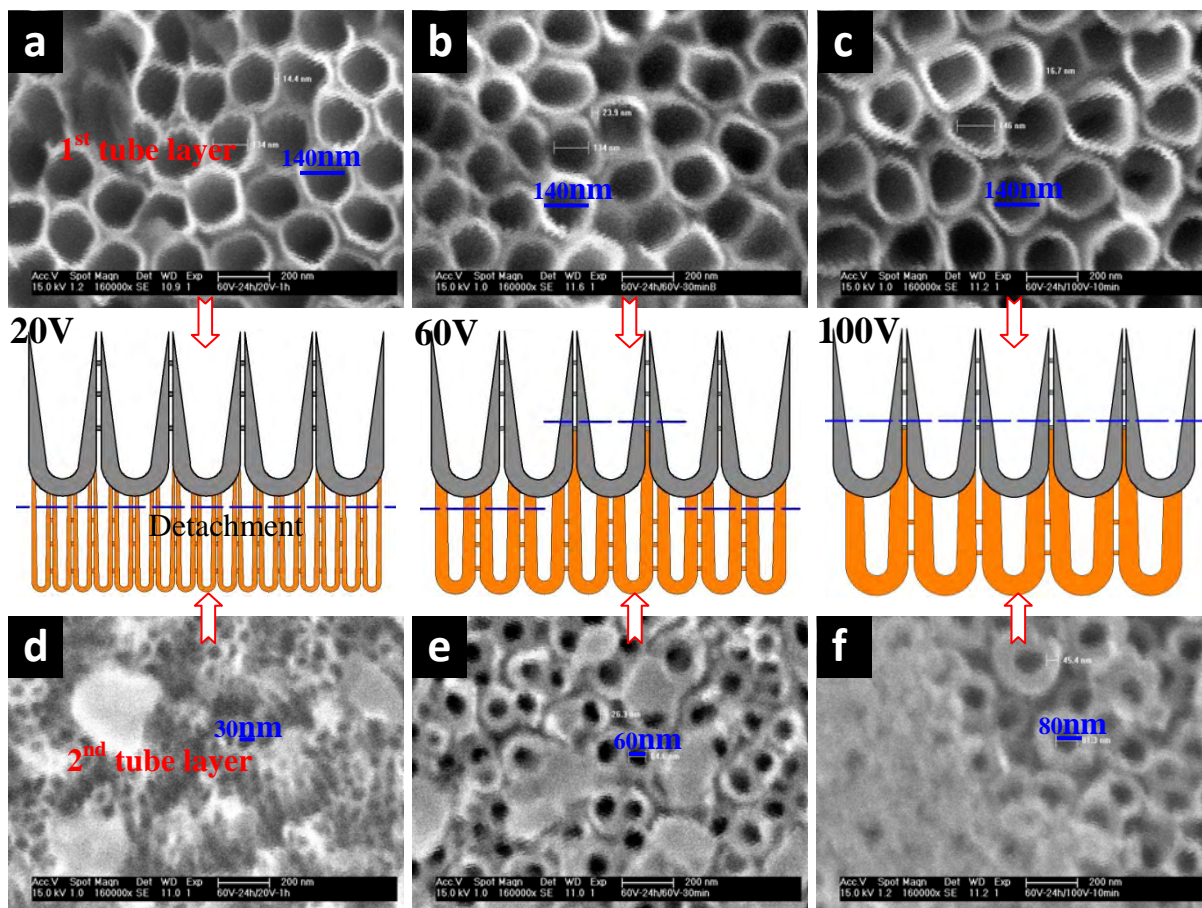
**Fig. 9.** The presumed structure before detachment, (a~c) top view images of the membrane and (d~f) the left layer on corresponding substrates.

X-ray diffraction (XRD) patterns were further used to characterize the crystal structure of the membranes. Standard patterns of Ti (JCPDS file 44-1294) and anatase TiO$_2$ (JCPDS file 84-1286) were plotted in Fig. 10 for comparison [71]. It shows that the preferential crystallographic orientation of the metallic Ti substrates is (103), the grain size of the underlying titanium substrate evaluated by Scherrer equation is about 194.8 nm. The as-prepared TNT film is amorphous and only diffraction peaks of Ti can be found in Fig. 10a. In general, as the annealing temperature increases from room temperature to 800 $^{\circ}$C, the phase of titanium oxide changes as amorphous→anatase→ rutile. To form anatase TiO$_2$, annealing at 330-500 $^{\circ}$C for 1-3h in an oxygen ambient is a common procedure in literatures [71, 77, 78]. After calcination at 500 $^{\circ}$C for 3 h, more X-ray diffraction patterns are clearly observed in Fig.10b, which can be referred to anatase phase.
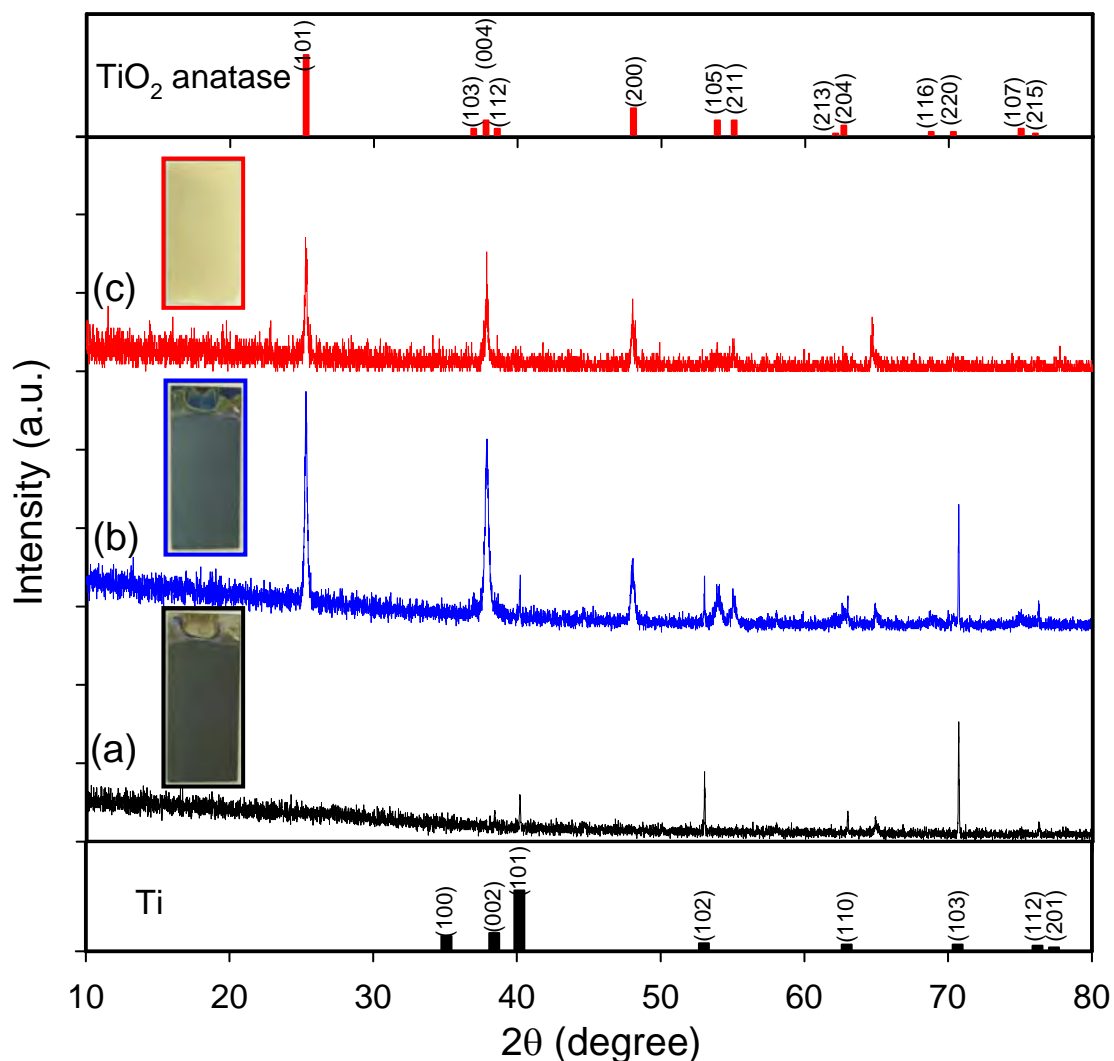
**Fig. 10.** XRD patterns of (a) as-prepared and (b) annealed TNT arrays on Ti substrates and (c) free-standing crystalline TNT membranes.

In contrast, for the crystallized free-standing TNT membrane, the diffraction peaks of Ti substrate disappear and all of the peaks can be attributed to the anatase $TiO_2$ phase (Fig. 10c), the strong diffraction peaks at $2\theta = 25.5^{\circ}$, $38.1^{\circ}$, $48.3^{\circ}$ can be identified, respectively, to the (101), (004), (200) crystal faces. The grain size of the anatase $TiO_2$ is about 81.6 nm, which was supposed no relevance to the grain size of the Ti foil but depended on the annealing temperature [69].

## 2.3  Photoconductive study of TiO₂ nanotubes

### 2.3.1  Photoconductive, free-standing crystallized TNT membranes (Article IV)

In this paper, we demonstrate that high photoconductive gain is achievable through a large-scale, free-standing crystallized TNT membrane. Schematic illustration of the

membrane fabrication via a two-step anodization and packaged device for the photoconductive characterization is shown in Fig.11. The first anodization grows ordered TNTs on a Ti foil, followed by annealing to crystallize the TNTs. Then, the annealed sample is anodized again to create an amorphous TNT layer below the crystallized layer, which is self-detached from the substrate to form a free-standing membrane. Next, the membrane is transferred to a silicon substrate patterned with gold interdigitated electrodes, and assembled with a quartz-glass cover to form a photoconductive device. The contribution of this work are (i) evidenced the controllable growth of free-standing TNT membranes, (ii) revealed the surface effects on the electrical transport in TNT membranes, (iii) extracted intrinsic properties of the TNTs from the effect of metal substrate and/or supporting electrolyte.
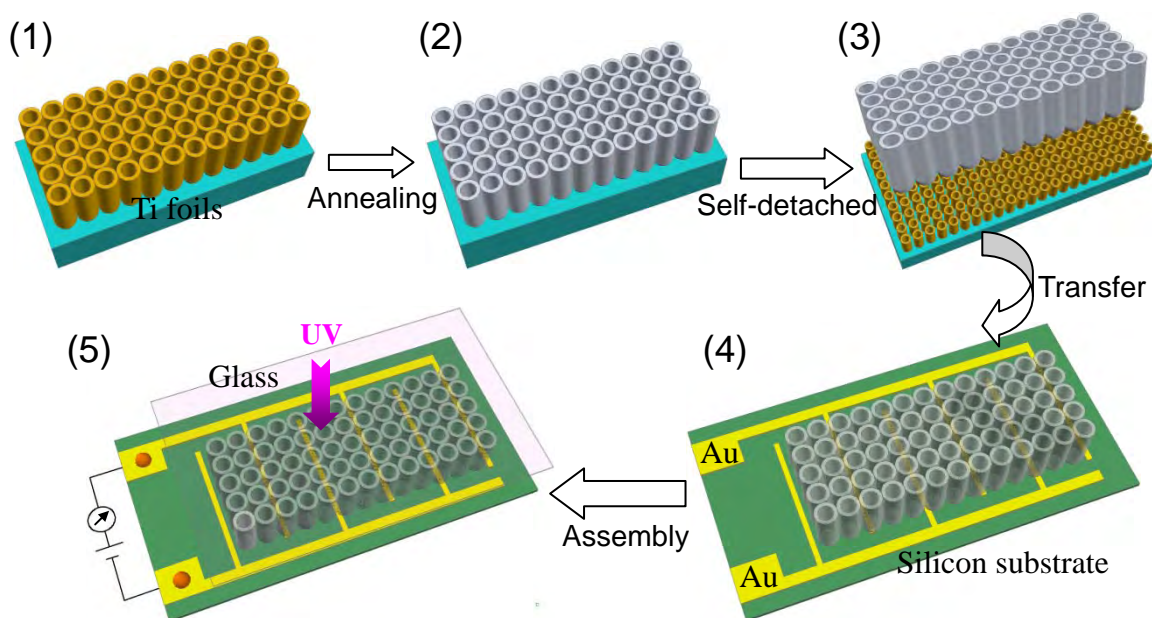


**Fig. 11.** Fabrication procedure (1) First anodization grows a layer of amorphous TNT. (2) Annealing the TNT layer. (3) Second anodization to grow a beneath layer of amorphous TNT and meanwhile detach the first layer. (4) Transfer the membrane to a substrate with gold electrodes. (5) A complete TNT-membrane device.

*Experimental Details*

*1. Synthesis of TNT membrane*

Ti foils were cut into an appropriate size (~12mm×35mm× 0.3mm, 99.8% purity), degreased and cleaned by sonication in acetone, isopropanol, and deionized water for 10 min during each step. After drying, the backside of Ti foil was covered by a Scotch tape, rinsed by water, and exposed to UV radiation about 10 min for cleaning. Then it was put into a polyflon cell with an area of 3.5 cm² exposed to the electrolyte. Ethylene glycol with 0.5 wt% ammonium fluoride (NH₄F) and 3.0 vol% water was used as electrolyte.

The first-step anodization was started with growth of ordered TNTs on Ti foil with various voltages as 20, 40, 60 and 80 V for 24 h, followed by sonic cleaning in ethanol to remove the electrolytes and annealing at 500 °C for 3 h to crystallize the TNTs. Then, the annealed samples were anodized again in the same stock electrolyte with another bias voltage of 100 V. When the detachment was observed (~10 min), the samples were picked out and rinsed by ethanol. The cleaned sample was then dried in air with the anodic surface facing up.

### 2. Photoconductive device fabrication

For photoconductive characterization, standard optical-lithography followed by Ti/Au (10/150 nm) deposition and liftoff were used to define the gold interdigitated electrodes on silicon substrate. The interdigital fingers are 0.8 mm wide, 11.5 mm long and interspaced by 2.0 mm. Then the TNT membrane was directly transferred onto the substrate, and covered by a piece of quartz glass with thickness ~ 0.5mm. Last, additional drops of glue on the partial boundary packaged the sandwich device. The membrane was physical interconnected/sandwiched between the Au-patterned substrate and the glass without using any adhesives. This is different from dye-sensitized solar cell structure, in which liquid electrolytes are required as electron carriers for solar to electrical conversion [79-81].

### 3. Characterization

The morphology and structural quality of membranes were investigated by scanning electron microscope (SEM, Philip EX-30) and transmission electron microscope (TEM, JEM-2010HR). The TNTs were scratched from the sample and dispersed in ethanol, and one drop of the suspension was dropped onto a carbon-coated copper grid for TEM measurements. The crystal structure was further identified by X-ray diffraction (XRD, Bruker AXS D8 Discover, Cu K$\alpha$ radiation). Transmission spectra were recorded with a DUV-vis spectrometer (Shimadzu SolidSpe-3700). Current-voltage (I-V) characteristics and the time responses of device to light irradiation were recorded with a Keithley 6430 source measure unit. A UV lamp (Tiede-50W switchable) with tunable intensity was selected as light source. The light intensity was measured with an OAI-306 power meter. All measurements were performed at room temperature in ambient conditions.

*Results and Discussion*

*1. Morphology and crystal structure of TNT membranes*

The as-prepared TNT membrane (~12 mm×30 mm) is mechanically robust and can be manipulated with a tweezers. The membrane appears white in color, free of cracks and with a small curvature after drying in air. This curvature is attributed to the absence of barrier layer at the bottom, where a compressive stress is existed [25]. Fig. 12 presents the dependence of diameter and thickness of the TNT membrane on applied voltage after 24 hours anodization. The pore diameter increases from 30 to 200 nm and the membrane thickness increases from 5 to 32 µm when the potential changes from 20 to 80 V. Low voltages (≤ 20V) result in an uncompleted surface oxidation process (Fig. 12a), while high applied voltage (≥80V) induces over-etching and produces disordered nanowires on the membrane surface (Fig. 12d). The optimal anodization voltage of the robust, free-standing membrane in the electrolyte is between 40~65V with a proper process period (~24 hours).
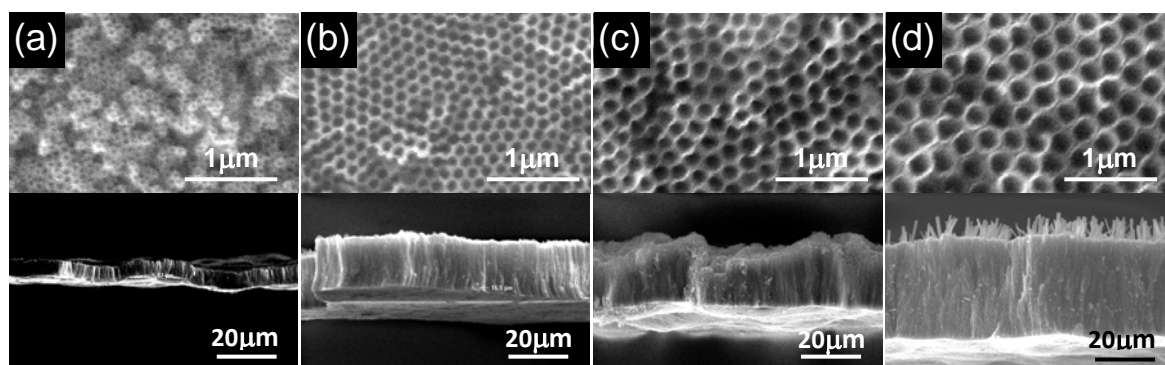


**Fig. 12.** Diameter and thickness of the membranes defined by the applied voltage in first anodization (a-d is 20, 40, 60, 80 V for 24 h anodization correspondingly, and detached at 20 V/1 h in the second anodization).

During the two-step anodization, applied voltage at the second anodization plays a critical role to define bottom morphology of the membrane. Membranes detached at low voltage (20V) retain nanotube morphology and the TNT bottom ends are closed. Through-hole membranes are obtained at a high detachment voltage (100 V) [13, 25, 34]. Fig. 13a-c present SEM images of the membrane fabricated at 60 V/24 hours and detached at 100 V/10 minutes. The top-view image shows an ordered and compact nanotube array rather than disordered structure (Fig. 13a). Average diameter of the constituted TNTs is 160 nm and the wall thickness on their mouth is ~12 nm. Dual-wall TNTs are observed at the bottom with uniform openings (Fig. 13b) and the pore diameter is ~50 nm. The thickness of the membrane is ~16 µm (Fig. 13c) with an

estimated aspect ratio of 100 (length/diameter). This vertically oriented, close-packed TNTs go straightly from the top to bottom which is important to supply a direct pathway for electron transportation in the nanostructure.
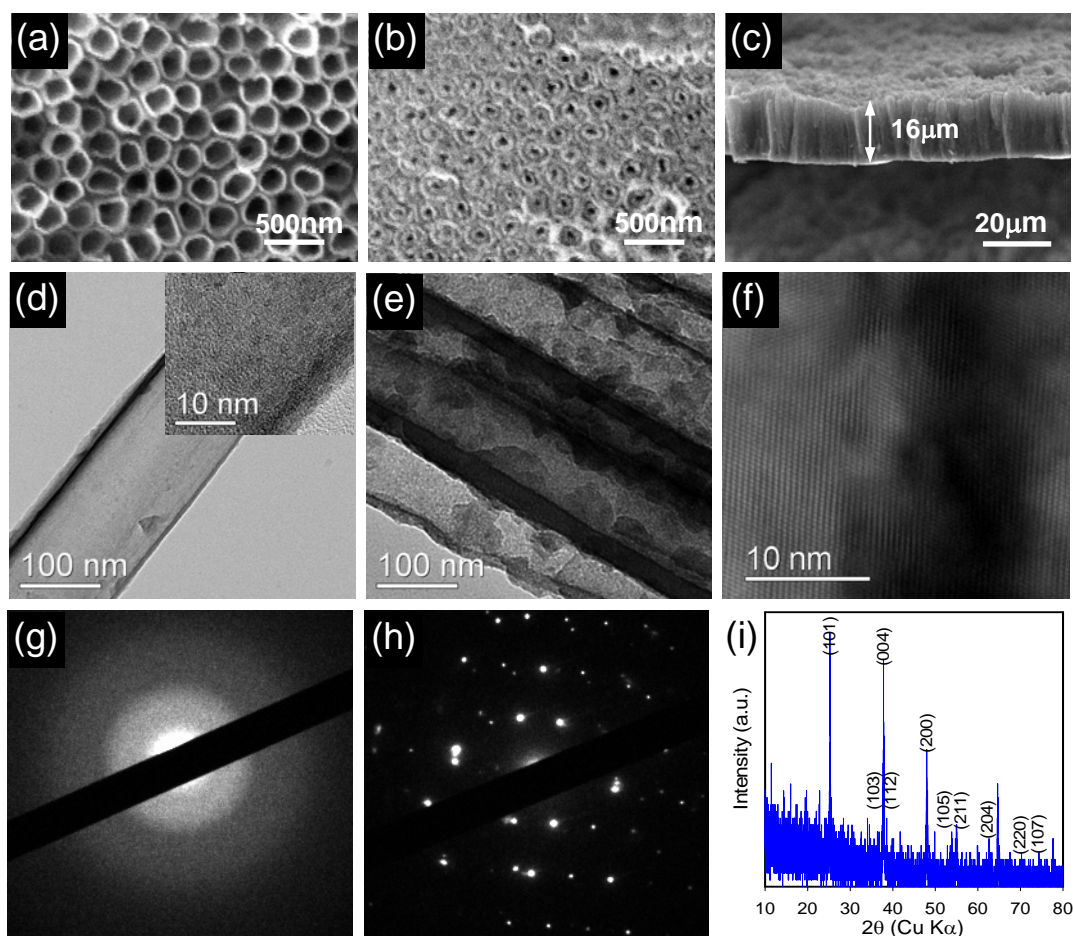


**Fig. 13.** SEM images of the TNT membrane (a) Top view. (b) Bottom view. (c) Cross-sectional view. TEM images of (d) single amorphous TNT and (e) crystalline TNTs. (f) TEM image shows crystalline order. (g) and (h) are selected area electron diffraction (SAED) pattern for the amorphous and the crystalline TNT. i) XRD patterns of the membrane.

Inspection of the as-prepared amorphous TNTs by using high resolution TEM (Fig. 13d and g) shows a disordered lattice characteristic. A large number of localized states in the amorphous structure act as traps and recombination centers, which degrades the TNT photo-catalytic/electronic performance [56, 78, 82, 83]. Crystallized and ordered structure is instantly apparent after annealing (Fig. 13e and f). The crystal lattice fringe spacing is 0.35nm corresponding to the spacing of (101) lattice plane of the anatase TiO₂ [71]. Selected area electron diffraction (SAED) pattern taken from a randomly chosen nanotube displays diffused rings (Fig. 13h). These rings indicate that the TNT membrane is polycrystalline. Meanwhile, XRD pattern (Fig. 13i) shows three strong diffraction peaks corresponding to the three isolated rings. All diffraction fringes are

indexed as the anatase $TiO_2$ phase (JCPDS file 84-1286), the diffraction peaks at $2\theta=25.5°$, $38.1°$, $48.3°$ are identified to be (101), (004), (200) crystal faces, respectively. The grain diameter estimated from TEM analysis is 80 nm while Scherrer analysis of the X-ray patterns gives a value of 82 nm from the (101) diffraction peak. The as-prepared amorphous TNTs crystallize initially as small grains, and then coalesce to form larger crystallites as the increasing of temperature [71]. However, the grain is not uniformly crystallized in TNTs, while the large size grains are formed on the location of thick wall with high local temperature [71, 83].

### 2. Photoelectrical measurement

Fig. 14a is a photograph of the packaged photoelectrical device for photoconductive characterization of the membranes, where Au electrodes on the silicon substrates are observed through the semi-transparency membrane (the sample in Fig. 13). Transmission spectrum of the free-standing TNT membrane was recorded between light wavelength 200-800 nm before assembly (Fig. 14b). It can be seen that the light is completely absorbed by the TNT membrane in the UV region below 330 nm (transmittance ~ 0%). In contrast, the transmittance reaches a value over 40% at wavelengths greater than 550 nm. It indicates that the membrane ensures selective absorption of UV light (< 330 nm) [3, 84].

Fig. 14c shows I-V characteristics of the TNT membrane device in dark and under UV illumination by a 320 nm light source at various intensities (5 minutes measurement for each case). The packaged photoelectrical device exhibits a nonlinear I-V curve due to the metal-semiconductor-metal structure [85, 86]. The near symmetric I-V curves indicate that there are two back-to-back contacts on the TNT membrane. At a fixed bias of 3.0 V, the photocurrents are about 11, 20 and 49 times larger than the dark current (1.8 µA) value when the system is illuminated by the UV light with intensity of 2.8 (20.5 µA), 12.5 (38.2 µA) and 42.0 (91.5 µA) mW/cm$^2$ respectively. The dependence of photocurrent on light intensity is plotted in the inset of Fig. 14c. The increases of photon induced current with increasing light intensity is arisen from the electron-hole pairs excited by the incident light which has an energy larger than the band gap [8, 86, 87]. It is consistent with the fact that the charge carrier photogeneration efficiency is proportional to the absorbed photon flux. The light power dependence is further fitted to a power law, $I_p \sim \Phi^{\theta}$, where $\theta$ determines the response of the photocurrent to light

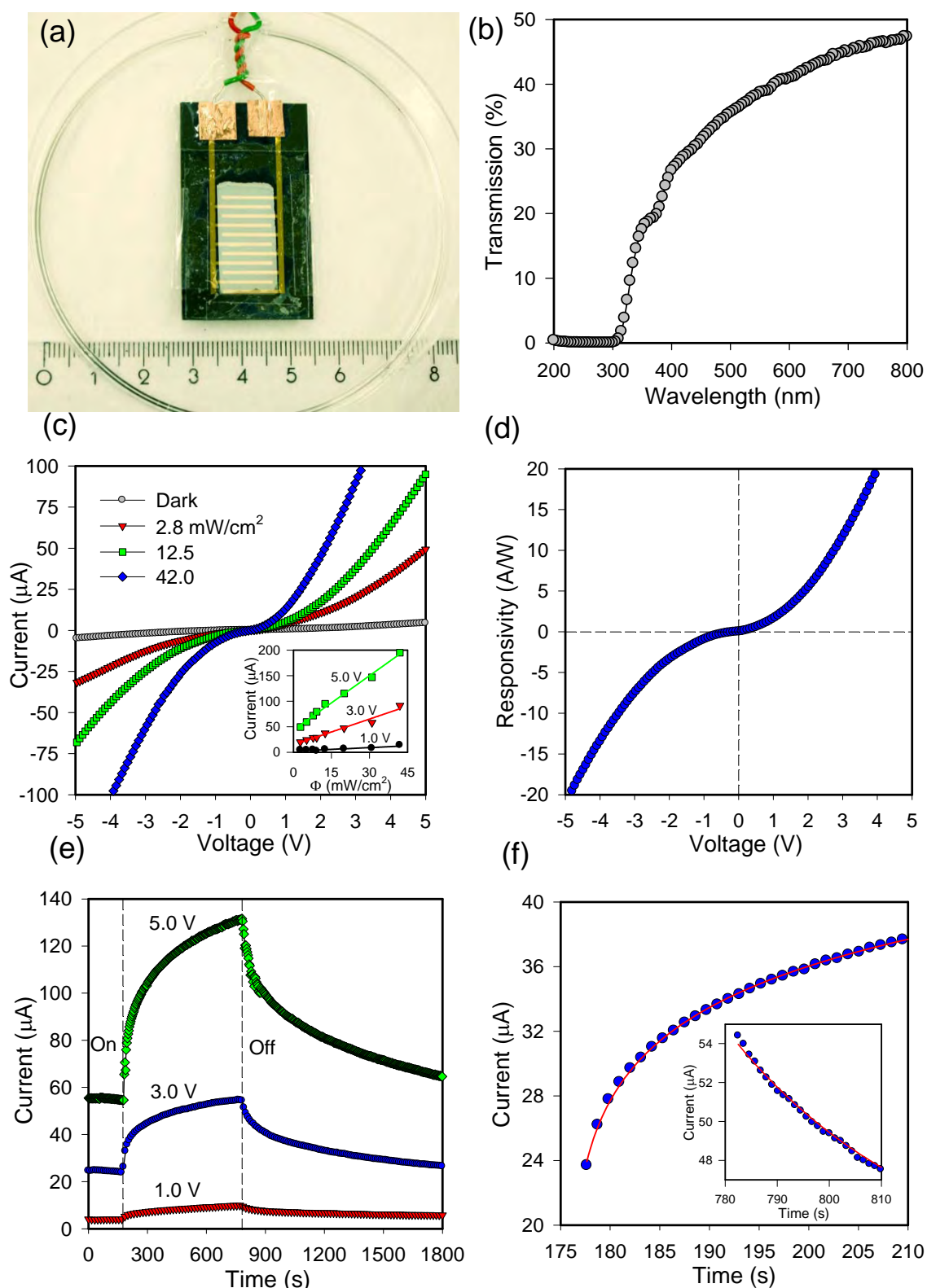**Fig. 14.** (a) A photo of the device. (b) Transmission spectra. (c) I-V characteristics of the device and the photocurrent as a function of intensity (inset). (d) The responsivity versus bias voltage. (e) Time-resolved photocurrent rise and decay obtained by sudden application (at 3 minutes) and removal (at 13 minutes) of light illumination $\Phi = 24.0$ mW/cm². (f) The growth and decay at 3.0 V bias.

intensity. The fitting gives a nearly linear behavior with $\theta = 0.65$ at bias 3.0 V. This non-unity ($0.5 < \theta < 1$) exponent suggests a complex process of electron-hole generation, recombination, and trapping within the membrane [88]. Fig. 14d displays the responsivity $R_\lambda = \Delta I / (\Phi S)$ versus applied-voltage under $\Phi = 12.5$ mW/cm². $\Delta I$ is the difference between the current under illumination and the dark current, S is the area of membrane, $\lambda$ is the wavelength of irradiated light [89]. The spectral response at 320 nm is ~30 A/W under 5.0V bias, corresponding to external quantum efficiency ($Q_E = hc R_\lambda / e\lambda$) ~10695%. In comparing with monolayer or nanosheets [87, 90], dense nanoparticulates /crystals devices [91-93] whose photocurrents are normally below 10 μA, our device provides a higher photocurrent ~200 μA at bias voltage of 5.0 V.

Fig. 14e shows photocurrent response during a 10-minute illumination pulse under biases of 1.0, 3.0 and 5.0 V. It is evident that applied bias voltage influences on/off ratio of the devices [94, 95]. At each bias, the initial current rises within 2 s under illumination as shown in Fig. 14f. The photocurrent rise is then followed by a slower component [96], in which the photocurrent increases in about 10 minutes before saturating. We observed plural time constants of the responsivity since the photocurrent response process generates a number of different classes of trap-states with different lifetimes [93]. The photocurrent decay starts with a fast component, during which the photocurrent is reduced in the first 2-10 s after turning off the excitation (inset of Fig. 14f). This fast decay process follows a first-order exponential relaxation function [96]. A further slow decay process lasts about tens of minutes before returning back to its initial dark-state.
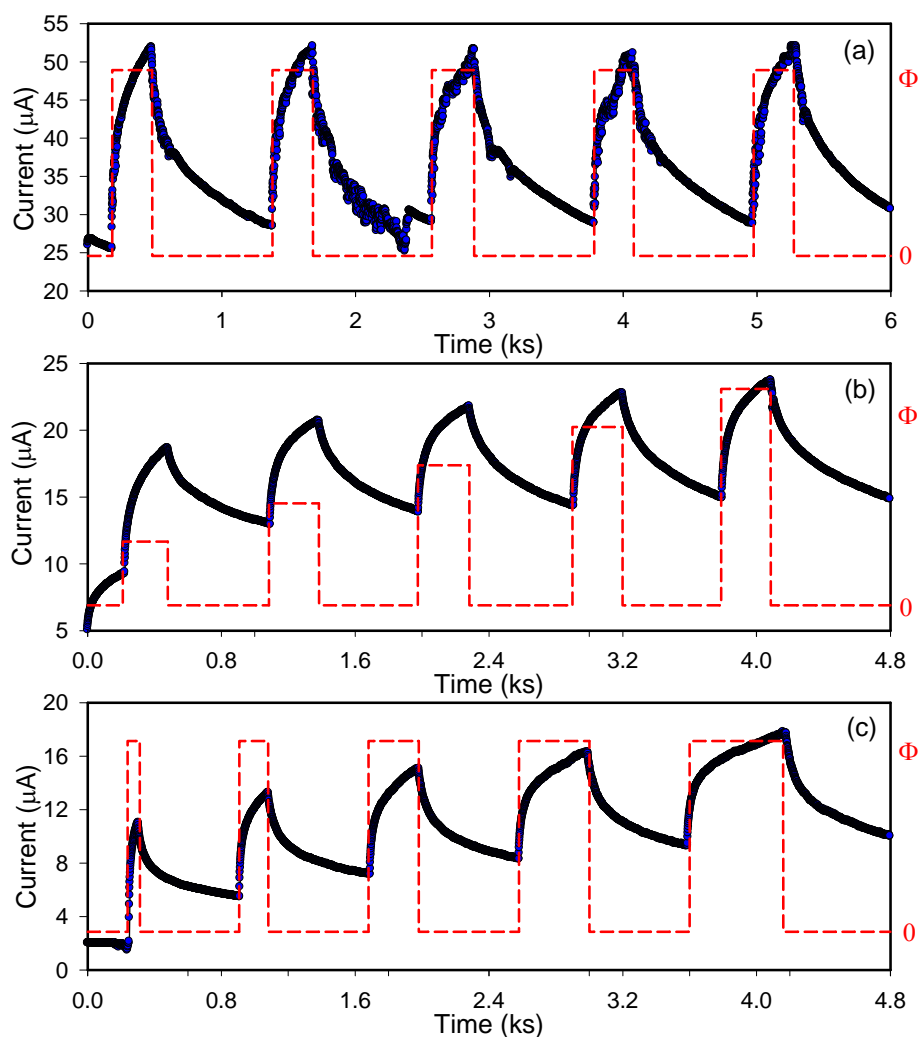
**Fig. 15.** Time-dependent photoresponse under pulse illumination (a) at 24.0 mW/cm$^2$ with 5 minnutes duration, (b) at different light intensities (5.0, 6.0, 7.0, 8.0, 9.0 mW/cm$^2$) with 5 minutes duration, (c) at 4.0 mW/cm$^2$ with various durations (1, 3, 5, 7, 9 minutes).

Fig. 15 shows reproducibility and stability of the TNT membranes under the bias of 3.0 V during repetitive switching of light illumination. The photocurrent increases to a value of 53 μA and then decreases to its initial level (Fig. 15a). After a given number of cycles, the photocurrent remains consistent, stable and reproducible. The origins of the observed current fluctuations are surface species absorption/desorption or appearance of defects [85]. The membrane response during tiny changes of light intensity and duration are depicted in Fig. 15b and c. The photocurrent increases with increasing intensity from 5.0 to 9.0 mW/cm$^2$ as well as extending duration from 1 to 9 minutes at 4.0 mW/cm$^2$. This increase is consistent with an increase of electron lifetime due to a reduction in the oxygen readsorption rate. It can be understood that the photocurrent gain depends on both the UV light intensity and duration, and the gain is accompanied by a slow decay [97].

*3. Inherent physical mechanism*

The optoelectronic measurements provide insight of charge transport in TNT membranes, including charge injection from gold contacts to the membrane and charge transport in the three dimensional TNT arrays [91, 97]. It is generally accepted that oxygen molecules are adsorbed onto the TNT surfaces by capturing free electrons from the semiconductor $[O_2(g)+e^-\rightarrow O^{2-}(ad)]$ (Fig. 16a), which creates a low-conductivity depletion layer near the surface [8, 84, 91, 98]. Upon UV excitation, electron-hole pairs are generated. The holes migrated to the surface along the potential gradient produced by band-bending either discharge the negatively charged adsorbed oxygen ions $[h^++O^{2-}\rightarrow O^2(g)]$ to photodesorb oxygen from the surfaces or get trapped at the TNT surfaces. This leads to an enhancement of carrier injection and transport, producing a persistent photocurrent [8, 95]. We note that the photocurrent response in our devices is larger
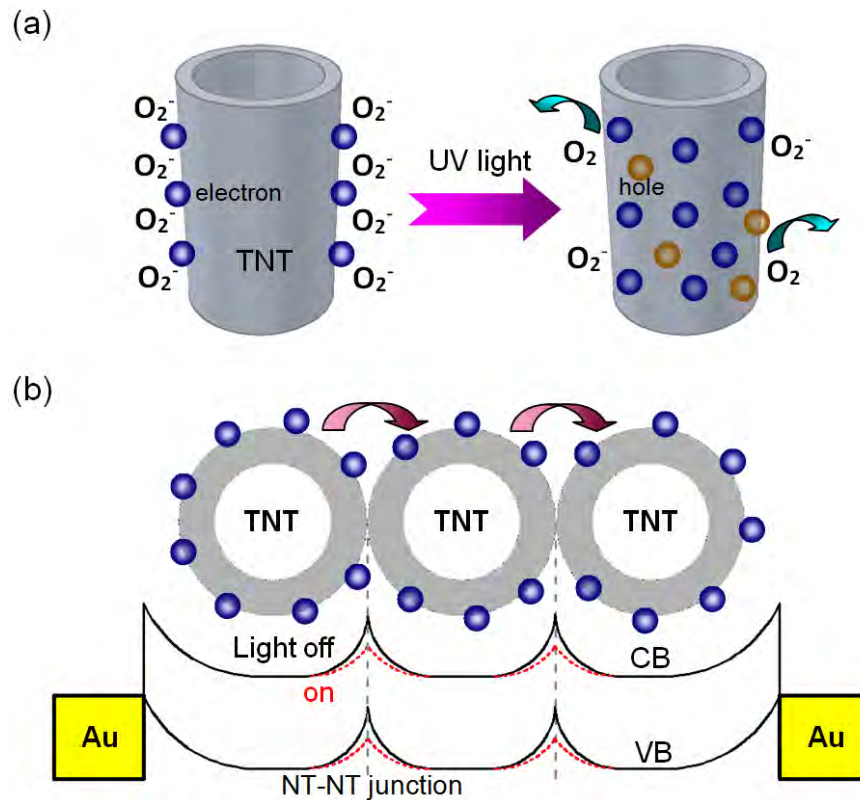


**Fig. 16.** Schematic illustration of (a) Oxygen adsorption in the dark and desorption under UV illumination. (b) The NT-NT junction barrier for electron transfer in the matrix, showing a decrease in NT-NT junction barrier height from the light-off state to light-on state.

(three orders) than the individual nanostructure-based devices whose photocurrent is in the range of several pA to nA [8, 86, 99]. As comparing with the immobilized membrane on Ti substrates, the absence of blocking layer on the membrane ensuring

perfect crystallinity and the large surface-to-volume ratio of the TNT increase the number of surface trap states, and facilitate oxygen adsorption / desorption at the surface. Compared to nanogranular films, oriented polycrystalline TNTs offer the advantage of directed electron transport, and are expected to have higher electron mobility. However, our data is inconsistent with this result. We assume that the slow photoresponse rise-drop speeds are caused by a single sharp resonance arising from exciton-like trap states [100]. Long spacing between electrodes in the devices extends the transport path of electrons and increases intercrystalline contacts, which also reduces the electron mobility [89, 101, 102]. Nevertheless, the device shows a high sensitivity to the UV light due to the existence of a percolated matrix. The electron conduction in the matrix is dominated by a combination of the grain-boundary barriers inside single nanotube and the junction barriers between neighboring tubes (NT-NT junction barriers) [86, 98]. Upon illumination, the carrier density in TNTs would narrow the barrier width or lower the effective barrier height (Fig. 16b), which facilitates an increase in electron transportation and results in an increase in conductivity of the TNT network [91, 98]. Since the light-induced barrier height modulation is much faster than the oxygen-diffusion, therefore the time response speed of the device is much fast in the first few seconds [71, 78, 96].

### 2.3.2 Small diameter TiO₂ nanotubes with enhanced photoresponsivity (Article V)

We report ultraviolet (UV) light detection of thin wall TiO₂ nanotubes (TNTs) with open diameter ~20 nm obtained by a two anodization procedure. This small diameter nanotubular geometry shows significant enhancement of the photoresponsivity and results in a large increase of photocurrent. The photocurrent is one order higher than that of classical nanotubes with diameter of 140 nm at -1.0 V bias. We attribute this improvement to the modulation of hole carrier density as a result of field effects from the diameter-dependent population of the surface-trapped electrons. This finding demonstrates inherent size effects of internal gain in semiconductor nanotubes.

*Experimental details*

The anodization was carried out in a two-electrode system. The setup details are described in reference [25]. For the growth of small diameter TNTs, a facile process was introduced (Fig. 17). First anodization was started with growth of TNTs on Ti foil ~60 V/24 h (Fig. 17 (1)), followed by annealing to crystallize the TNTs (Fig. 17 (2)). Then,

the annealed samples were anodized again with another small voltage (20V). When the detachment of the first layer TNTs was completed over time ~1 h (Fig. 17 (3)), the substrate was picked out and rinsed by ethanol. Last, the substrate was annealing again to crystallize the small diameter TNTs (Fig.17 (4)). To grow a conventional large diameter TNTs ~140 nm for reference, one-step anodization was performed at 60 V for 1 h.
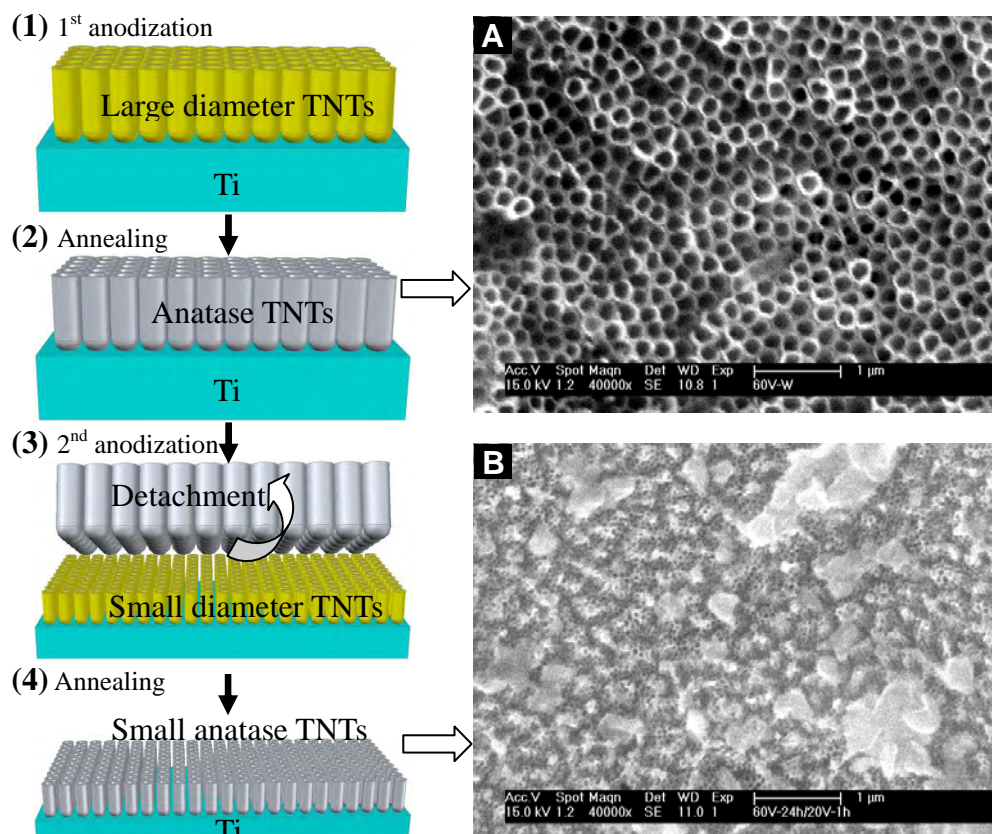


**Fig. 17.** The fabrication procedure (A) large diameter and (B) small diameter nanotubes.

The morphology and structural quality of the TNTs were investigated by SEM (Philip EX-30) and TEM (JEM-2010HR). The nanotubes were scratched from the Ti metal substrate, dispersed in ethanol and then transferred to copper grids for TEM tests. X-ray diffraction analysis (Bruker AXS D8 Discover with a normal θ-2θ scan, Cu-Kα radiation) was performed for phase identification. To characterize photoresponsivity of the crystallized TNTs, FTO glass was integrated on the surface of TNT films to form photoconductive devices. Current-voltage (I-V) curves and time responses of the devices to light irradiation were recorded with a Keithley 6430 source measure unit. A UV lamp (Tiede-50W, λ=320nm switchable) with tunable light intensity was selected as light source. The light intensity was measured with an OAI-306 power meter.

*Results and discussion*

Fig. 17-A shows a top-view SEM image of the large diameter TNTs grown at 60 V for 1h. It is evident that the ordered nanotube array consists of well-aligned nanotubes with an average inner diameter of 140 nm and wall thickness ~15 nm. The image of small diameter TNTs fabricated by the two anodization step, as shown Fig. 17-B, indicates that the TNTs remain compact and no destructive changes after detaching the first crystalline layer. The constituted TNTs are of an average diameter of 20 nm with a thin wall ~ 5 nm. During second anodic step, the first crystalline TNT layer serves as a buffer for reducing the strength of electrical field and to protect the new formed nanotubes from chemical dissolution. Thus, uniform and small diameter nanotubes are realized after the second anodization at 20 V for 1 hour [103]. These close-packed, small diameter nanotube arrays provide a direct pathway for electron transport at the nanotube walls. Minor bottom parts of the first tube layer left on the small diameter tubes, which serves as the electron transporter for effective charge separation and rapid transport of the photogenerated electrons [104].

As the annealing temperature increases from room temperature to 800 °C, the phase of as-prepared TNTs is changed as amorphous→ anatase → rutile. The TNT morphology is collapsed at temperature above 600 °C. To form anatase TNT with preferred morphology and higher photoelectric activity, annealing at 350~500 °C for 2-3 h in oxygen ambient is a reasonable temperature process [8, 25, 78, 105]. The TEM image and selected-area electron diffraction (SAED) pattern of the TNTs are shown in Fig. 18. The high resolution TEM image shows a disordered characteristic for as-prepared amorphous TNTs (Fig. 18(a)). Crystallized and ordered structures of the nanotubes are observed after annealing at 500 °C for 3 h (Fig. 18(b)). The image reveals distinctive lattice fringes spaced by 0.35 nm and exhibits anatase-type polycrystalline Debye-Scherrer rings in the upper-right inset. XRD pattern (Fig. 18(c)) further confirms that the as-prepared TNT is amorphous and only diffraction peaks of Ti substrate are detected (JCPDS file 44-1294). On the contrary, the crystallized counterpart shows three strong diffraction peaks corresponding to the three isolated rings. All reflections are indexed (JCPDS file 84-1286), and the diffraction peaks at $2\theta=25.5°$, $38.1°$, $48.3°$ are identified to be the (101), (004), (200) crystal faces respectively. There is no significant change in the pore diameter or wall thickness after annealing.
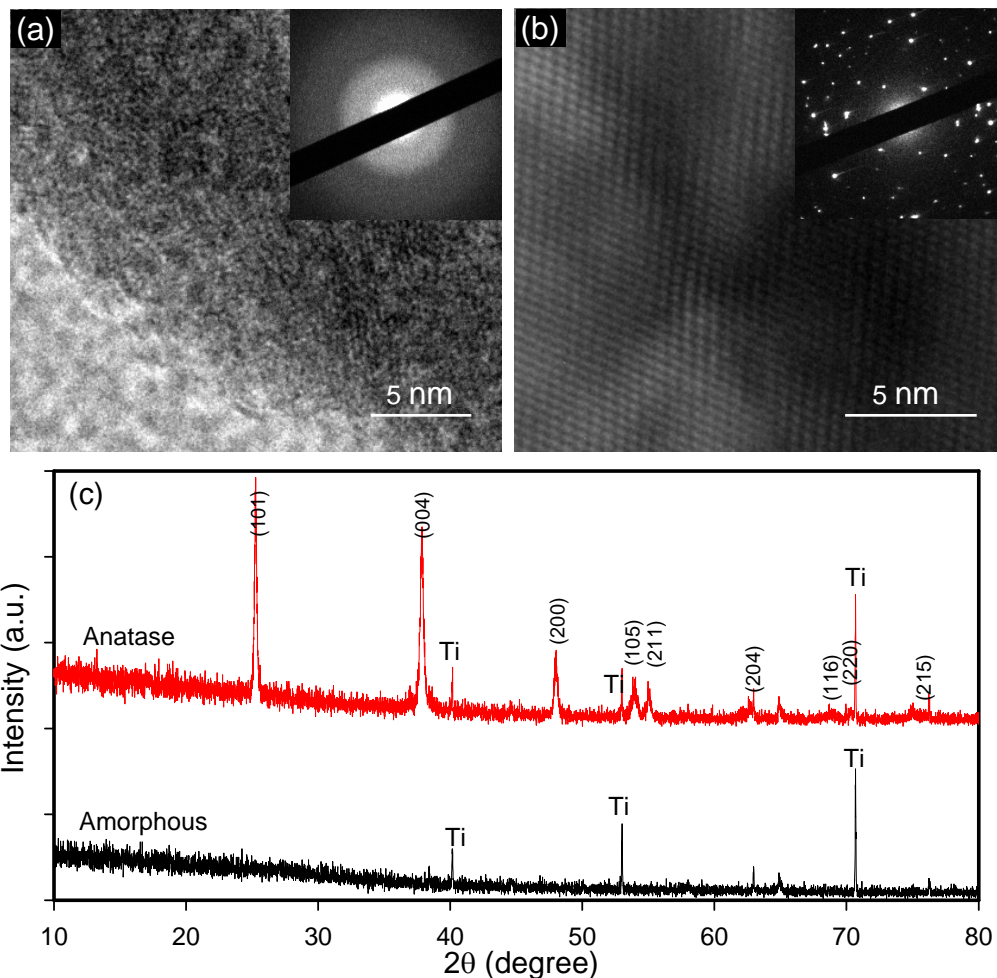
**Fig. 18.** TEM characterizations of (a) amorphous and (b) anatase TNTs (c) XRD patterns.

To extract the size-dependent photoelectrical properties of the crystallized TNTs, a FTO/TNT/Ti photoconductive device is then assembled, as schematically shown in the inset of Fig. 19(a). Two sets of linear sweep voltammograms are recorded in Fig. 19(a) under both dark and UV illumination of 5 mW/cm². I-V curves present linear dependence with the applied bias at forward region while it exhibits a nonlinear behavior with the reverse bias. In particular, with the reverse bias, the FTO/TNT/Ti heterojunction gives a better photoresponsivity with large ratios ($I_{photo}/I_{dark}$) approximately 735 (Sample B) and 27 (Sample A) at -1.0 V. We assume that the photoresponse is likely to be dominated by the Ti/TiO₂ heterojunction area. Both samples show small dark current on the order of ~ 10 μA. The sample A keeps a larger dark current with the reverse bias, indicating the background current of devices is relevance to the sign and intensity of the external electric field. The device of the small diameter nanotubes not only shows pronounced photoresponse under light illumination, but also exhibits even higher photocurrent. The maximum photocurrent is 7.5 μA at 0.2 V, which is about 6 times larger than that ~1.2 μA for sample A. Similar enhancement of photoresponsivity is observed with a small reverse bias -0.1 V (Fig. 19(b)). This confirms a better interfacial charge transfer occurred in small diameter TNTs. Fig. 19(c)

represents the photoresponse of the both samples at bias of 0.2 V, where the photocurrent is plotted as a function of time with light intensities from 5.0 to 3.8 mW/cm$^2$. The light source is repetitively switched on/off with a reducing-step of 0.2mW/cm$^2$ to witness the reproducibility of the data versus time.
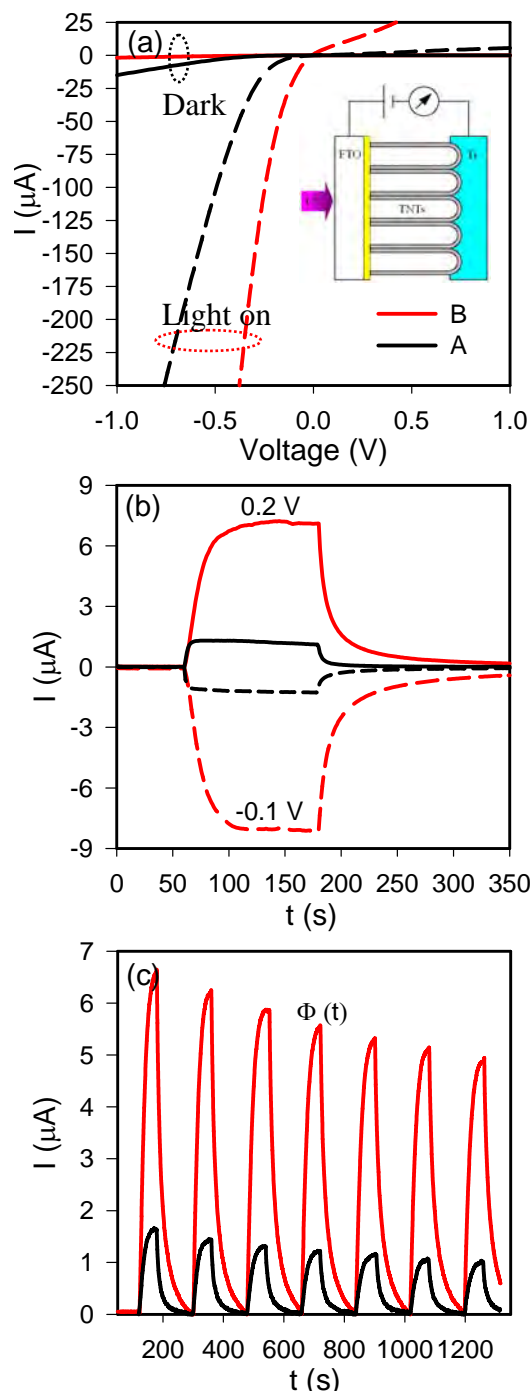
**Fig. 19.** (a) I-V curves in dark and illumination, (b) photoresponses with different biases, (c) time dependent photoresponses

It can be seen that the device behaves well under continuous cycling. The photocurrent decreases even with tiny fluctuation of light intensity, which the photocurrent gain is largely dependent on the light intensity.

The irradiation induced conductivity $\Delta\sigma$ (photoconductivity) occur either due to a change in the carrier concentration $\Delta n$ (carrier photogeneration) or to a change in the carrier mobility $\Delta\mu$ [51, 52, 106, 107]. $\Delta n \gg \Delta\mu$ and the time dependence of the mobility is negligible. The photocurrent reduces to the usual form $I_{photo} = \Delta\sigma_{photo}EA = e\mu\Delta n_{eff}(d)EA$, where $e$ is the electronic charge, $d$ is the nanotube diameter, $E$ is the applied electric field and $A$ is the area. The field effect from the trapped holes at the TNT surfaces is diameter-dependent. The effective carrier density modulation can be expressed as $\Delta n_{eff}(d) = \Delta n + \Delta n_{acc}(d)$ [51, 52, 100]. The number of the electron-hole pairs created at a tube cross section per unit length is proportional to $\pi(d_o^2 - d_i^2)/4$, the number of surface trapped holes per unit length is proportional to $\pi(d_o + d_i)$, where $d_o$ and $d_i$ is outer and inner wall diameter of TNT respectively. Provided that the induced electron concentration is directly proportional to the number of surface-trapped holes by an electrostatic interaction, the accumulated hole concentration is expressed by $\Delta n_{acc} \propto \dfrac{4\pi(d_o + d_i)}{\pi(d_o^2 - d_i^2)} \propto \dfrac{1}{d_o - d_i} \propto \dfrac{1}{\delta}$, $\delta$ is the wall thickness [51, 52]. It means that the accumulated hole concentration is inversely proportional to the wall thickness. So we should obtain $\sim 3$ times difference in $\Delta n_{acc}$ between the two nanotubes, which is qualitatively consistent with the variation of the observed photocurrent (see Fig.19 (b)-(c)). In this experiment, the thickness of large and small diameter tubes (evaluated from the growth rate at 60 and 20V) is $\sim 680$ and $200$ nm, respectively. Long tube length extends the transport path of electrons and increases intercrystalline contacts, which decreases the electron mobility [4, 108]. The decrease in diameter and wall thickness of nanotubes enhances the specific surface area, so that the dissociation efficiency of excitons and the accumulated electron concentration increases [51, 54, 109]. Therefore, the large specific surface area and a fast transport path for carriers are the main advantages of small diameter nanotubes as compared to large ones. The field effect from the diameter-dependent population facilitates an increase in electron transportation and results in a significant increase of photoresponsivity in the small diameter TNTs.

# 3  Conclusions

This thesis aims to develop cutting-edge technology for reliable fabrication of TNT membranes. Materials formation mechanisms and their photoconductive properties have been investigated systematically. The main conclusions are drawn in the following aspects:

- A simple process was developed for fabricating amorphous TNT membranes. The anodization voltage is critical for the detachment through regulating the migration of fluoride ions on the barrier. Rinsing the as-prepared TNT membranes by pure ethanol prevents morphological disorder induced by capillary stress and results in a clean surface with ordered nanostructure. Reducing the rate of ethanol evaporation by covering an additional cleanroom paper on the as-anodized substrates is a key step to prepare a large scale and flat surface TNT membranes.

- A voltage-dependent investigation was performed for the detachment process of free-standing crystalline TNT membranes. Crystallized TNT membranes with high ordered nanotubes were effectively detached from the substrate by taking advantage of different mechanical stability between the layers. The membrane detached at low voltage preserves its nanotube morphology and the bottom of tubes are closed, while through-hole membrane with fast detachment can be obtained at a high detachment voltage.

- TNT membranes were synthesized by a two-step anodic procedure, in which dependence of the TNT morphology on the applied voltage is experimentally present. Due to the large surface area-to-volume ratio and high quality crystal structure, the membrane exhibits a sensitive spectral response to the ultra violet (UV) light. The photoresponse origins from internal gain induced by desorption of oxygen molecules from the nanotube surfaces and reduction of the barrier at neighboring tubes under UV illumination.

- We compare the UV light sensitivity between the small diameter ~20 nm and the conventional diameter TNTs. The small diameter nanotube device enhances the UV photoresponsivity and leads to a larger increase of photocurrent. The photocurrent value increases ~3 orders of magnitude when the light switches from off to on status. These observations is associated with the modulation of hole carrier density, which comes from field effects of the diameter-dependent population of the electrons.

This work provides powerful approach to tailor the properties of self-organized TNTs, which may have far-reaching implications in the design of future nanoscale systems. The progress together with emerging methods for deterministic assembly, leads to compelling opportunities for research from basic studies of two-dimensional physics to the development of applications such as optoelectronic or photovoltaic devices, photocatalysis, nano-template and sensors etc.

# References

[1] K. Shankar, J. I. Basham, N. K. Allam, et al., Recent advances in the use of $TiO_2$ nanotube and nanowire arrays for oxidative photoelectrochemistry, J. Phys. Chem. C 2009, 113, 6327-6359.

[2] G. K. Mor, K. Shankar, M. Paulose, O.K. Varghese, C.A. Grimes, Enhanced photocleavage of water using titania nanotube arrays, Nano Lett. 5 (2005) 191-195.

[3] G. K. Mor, O. K. Varghese, M. Paulose, K.Shankar, C.A. Grimes, A review on highly ordered, vertically oriented $TiO_2$ nanotube arrays: Fabrication, material properties, and solar energy applications, Sol. Energy Mater. Sol. Cells. 90 (2006) 2011-2075.

[4] P. Roy, D. Kim, K. Lee, E. Spiecker, $TiO_2$ nanotubes and their application in dye-sensitized solar cells, P. Schmuki, Nanoscale 2 (2010) 45-59.

[5] S. Devipriya, S. Yesodharan, Photocatalytic degradation of pesticide contaminants in water, Sol. Energy Mater. Sol. Cells 86 (2005) 309-348.

[6] U.I. Gaya, A.H. Abdullah, Heterogeneous photocatalytic degradation of organic contaminants over titanium dioxide: A review of fundamentals, progress and problems, J. Photochem. Photobiol. C 9 (2008) 1-12.

[7] M. Paulose, O. K. Varghese, G. K. Mor, C.A. Grimes, K. G. Ong, Unprecedented ultra-high hydrogen gas sensitivity in undoped titania nanotubes, Nanotechnology 17 (2006) 398-402.

[8] J. Zou, Q. Zhang, K. Huang, N. Marzari, Ultraviolet photodetectors based on anodic $TiO_2$ nanotube arrays, J. Phys. Chem. C, 114(2010)10725-10729.

[9] P. Roy, S. Berger, and P. Schmuki, $TiO_2$ Nanotubes: Synthesis and Applications, Angew. Chem. Int. Ed. 50 (2011) 2904-2939.

[10] C. A. Grimes, G. K. Mor, $TiO_2$ nanotube arrays synthesis, properties, and applications, Springer, New York, 2009, ISBN 978-1-4419-0067-8.

[11] D. Gong, C. A. Grimes, O. K. Varghese, Titanium oxide nanotube arrays prepared by anodic oxidation, J. Mater. Res., 16 (2001)3331-3334.

[12]   M. Paulose, H. E. Prakasam, O. K. Varghese, L. Peng, K. C. Popat, G. K. Mor, T.A. Desai, C. A. Grimes, TiO$_2$ nanotube arrays of 1000  m length by anodization of titanium foil: phenol red diffusion, J. Phys. Chem. C. 111 (2007) 14992-14997.

[13]   G. Liu, K. Wang, N. Hoivik, H. Jakobsen, Progress on free-standing and flow-through TiO$_2$ nanotube membranes, Sol. Energy Mater. Sol. Cells. 98 (2012) 24-38.

[14]   B.X. Lei, J.Y. Liao, R. Zhang, J. Wang, C.Y. Su, D.B. Kuang, Ordered crystalline TiO$_2$ nanotube arrays on transparent FTO glass for efficient dye-sensitized solar cells, J. Phys. Chem. C. 114 (2010) 15228-15233.

[15]   Q. Zheng, H. Kang, J. Yun, J. Lee, J.H. Park, S. Baik, Hierarchical construction of self-standing anodized titania nanotube arrays and nanoparticles for efficient and cost-effective front-illuminated dyesensitized solar cells, ACS Nano 5 (2011) 5088-5093.

[16]   C.J. Lin, W.Y. Yu, Y.T. Lu, S.H. Chien, Fabrication of open-ended high aspect-ratio anodic TiO$_2$ nanotube films for photocatalytic and photoelectrocatalytic applications, Chem. Commun. (2008) 6031- 6033.

[17]   Q.W. Chen, D.S. Xu, Z.Y. Wu, Z.F. Liu, Free-standing TiO$_2$ nanotube arrays made by anodic oxidation and ultrasonic splitting, Nanotechnology 19 (2008) 365708 (5pp).

[18]   O.K. Varghese, M. Paulose, T.J. LaTempa, C. A. Grimes, High-rate solar photocatalytic conversion of CO$_2$ and water vapor to hydrocarbon fuels, Nano Lett. 9 (2009) 731-737.

[19]   K. Yu , W. Yu, M. Kuo, Y. Liou, S. Chien, Pt/titania-nanotube: A potential catalyst for CO$_2$ adsorption and hydrogenation, Appl. Catal. B: Environ. 84 (2008) 112-118.

[20]   S.P. Albu, A. Ghicov, J.M. Macak, R. Hahn, P. Schmuki, Self-Organized, free-standing TiO$_2$ nanotube membrane for flow-through photocatalytic applications, Nano Lett. 7 (2007) 1286-1289.

[21]   B. Zhu, J.J. Li, Q.W. Chen, R.G. Cao, J.M. Li, D.S. Xu, Artificial, switchable K$^+$-gated ion channels based on flow-through titania-nanotube arrays, Phys. Chem. Chem. Phys. 12 (2010) 9989-9992.

[22]   J. Lin, J.F. Chen, X.F. Chen, Facile fabrication of free-standing TiO$_2$ nanotube membranes with both ends open via self-detaching anodization, Electrochem. Commun. 12 (2010) 1062-1065.

[23]    K. Kant, D. Losic, A simple approach for synthesis of TiO$_2$ nanotubes with through-hole morphology, Phys. Status Solidi RRL. 3 (2009) 139-141.

[24]    S. Banerjee, M. Misra, S. K. Mohapatra, C. Howard, S.K. Mohapatra and S. K. Kamilla, Formation of chelating agent driven anodized TiO$_2$ nanotubular membrane and its photovoltaic application, Nanotechnology 21 (2010) 145201(9pp).

[25]    G.H. Liu, N. Hoivik, K.Y. Wang, H. Jakobsen, A voltage-dependent investigation on detachment process for free-standing crystalline TiO$_2$ nanotube membranes, J. Mater. Sci. 46 (2011) 7931-7935.

[26]    V. K. Khanna, Adhesion-delamination phenomena at the surfaces and interfaces in microelectronics and MEMS structures and packaged devices, J. Phys. D: Appl. Phys. 44 (2011) 034004 (19pp).

[27]    J.W. Ng, X.W. Zhang, T. Zhang, Construction of self-organized free-standing TiO$_2$ nanotube arrays for effective disinfection of drinking water, J Chem. Technol. Biotechnol. 85 (2010) 1061-1066.

[28]    J. Wang, Z. Lin, Freestanding TiO$_2$ nanotube arrays with ultrahigh aspect ratio via electrochemical anodization, Chem. Mater. 20 (2008) 1257-1261.

[29]    X. Meng, T.Y. Lee, H. Chen, D.W. Shin, K.W. Kwon, S.J. Kwon, J.B. Yoo, Fabrication of free standing anodic titanium oxide membranes with clean surface using recycling process, J. Nanosci. Nanotechno. 10 (2010) 4259-4265.

[30]    D. Fang, K.L. Huang, S.Q. Liu, Z.P. Luo, X.X. Qing, Q.G. Zhang, High-density NiTiO$_3$/TiO$_2$ nanotubes synthesized through sol-gel method using well-ordered TiO$_2$ membranes as template, J. Alloys Compd. 498 (2010) 37-41.

[31]    D. Fang, K.L. Huang, S.Q. Liu, D.Y. Qin, High density copper nanowire arrays deposition inside ordered titania pores by electrodeposition, Electrochem. Commun. 11 (2009) 901-904.

[32]    Y. Shin, S. Lee, A free standing membrane of highly ordered anodic ZrO$_2$ nanotube arrays, Nanotechnology 20 (2009) 105301(5pp).

[33]    S. Singh, M. Festin, W.R.T. Barden, L. Xi, J.T. Francis, P. Kruse, Universal method for the fabrication of detachable ultrathin films of several transition metal oxides, ACS Nano. 2 (2008) 2363-2373.

[34]    D.A. Wang, L.F. Liu, Continuous fabrication of free-standing TiO$_2$ nanotube array membranes with controllable morphology for depositing interdigitated heterojunctions, Chem. Mater. 22(2010) 6656-6664.

[35]    Y. Jo, Jung I, I. Lee, J. Choi, Y. Tak, Fabrication of through-hole TiO$_2$ nanotubes by potential shock, Electrochem. Commun. 12 (2010) 616-619.

[36]    S. LI, G. Zhang, One-step realization of open-ended TiO$_2$ nanotube array by transition of the anodizing voltage, Journal of the Ceramic Society of Japan 118 (2010) 291-294.

[37]    Q.W. Chen, D.S. Xu, Large-Scale, noncurling, and free-standing crystallized TiO$_2$ nanotube arrays for Dye-sensitized solar cells, J. Phys. Chem. C 113 (2009) 6310-6314.

[38]    K. Li, Z. Xie, S. Adams, K.Li, Z. Xie, A reliable TiO$_2$ nanotube membrane transfer method and its application in photovoltaic devices, Electrochimica Acta 62 (2012) 116-123.

[39]    S. Yoriya, M. Paulose, O.K. Varghese, G.K. Mor, C.A. Grimes, Fabrication of vertically oriented TiO$_2$ nanotube arrays using dimethyl sulfoxide electrolytes, J. Phys. Chem. C. 111 (2007) 13770-13776.

[40]    Q.S. Zhong, D.W. Wang, F. Li, G.Q. Lu, H.M. Cheng, Preparation of free-standing transparent titania nanotube array membranes, Chinese journal of materials research. 23 (2009) 118-122.

[41]    C.J. Lin , Y.H. Yu , Y.H. Liou, Free-standing TiO$_2$ nanotube array films sensitized with CdS as highly active solar light-driven photocatalysts,  Appl. Catal. B: Environ. 93 (2009) 119-125.

[42]    M. Dubey, M. Shrestha, Y. Zhong, D. Galipeau, H. He, TiO$_2$ nanotube membranes on transparent conducting glass for high efficiency dye-sensitized solar cells, Nanotechnology 22 (2011) 285201 (9pp).

[43]    J.H. Park, T.W. Lee,  M.G. Kang, Growth, detachment and transfer of highly-ordered TiO$_2$ nanotube arrays: use in dye-sensitized solar cells, Chem. Commun. (2008) 2867-2869.

[44]    D.A. Wang, Y. Liu, B. Yu, F. Zhou, W.M. Liu, TiO$_2$ Nanotubes with tunable morphology, diameter, and length: synthesis and photo-electrical/catalytic performance, Chem. Mater. 21 (2009) 1198-1206.

[45]    D.A. Wang, B.Yu, C.W. Wang, F. Zhou, W.M. Liu, A novel protocol toward perfect alignment of anodized TiO$_2$ nanotubes,  Adv. Mater. 21 (2009) 1964-1967.

[46]    S.P. Albu, A. Ghicov, S. Berger, H, Jha, P. Schmuki, TiO$_2$ nanotube layers: flexible and electrically active flow-through membranes, Electrochem. Commun. 12 (2010) 1352-1355.

[47]    Z. Zhang, D. Guo, Y. Xing, G. Zhang, Fabrication of open-ended TiO₂ nanotube arrays by anodizing a thermally evaporated Ti/Au bilayer film, Appl. Surf. Sci. 257 (2011) 4139-4143.

[48]    L.L. Li, Y.J. Chen, H.P. Wu, N.S. Wang, E.W. Diau, Detachment and transfer of ordered TiO₂ nanotube arrays for front-illuminated dye-sensitized solar cells, Energy Environ. Sci. 4(2011)3420-3425.

[49]    G. Konstantatos, E.H. Sergeant, nanostructured materials for photon detection, Nat. Nanotechnol. 5 (2010) 391-400.

[50]    L. Cao, J. S. White, J. Park, J. A. Schuller, B.M. Clemens, M.L. Brongersma, Engineering light absorption in semiconductor nanowire devices, Nat. Mater. 8 (2009) 643-647.

[51]    C. J. Kim, H. S. Lee, Y. J. Cho, K. Kang, M. H. Jo, Diameter-dependent internal gain in Ohmic Ge nanowire photodetectors, Nano Lett. 10 (2010) 2043-2048.

[52]    Q. Zhang, J. Qi, X. Li, Y. Zhang, Diameter-dependent internal gain in ZnO micro/nanowires under electron beam irradiation, Nanoscale 3 (2011) 3060-3063.

[53]    R. S. Chen, C. A. Chen, H. Y. Tsai, W. C. Wang, Y. S. Huang, Photoconduction properties in single-crystalline titanium dioxide nanorods with ultrahigh normalized gain, J. Phys. Chem. C 116 (2012) 4267-4272.

[54]    M. Ouyang, R. Bai, L. Yang, Q. Chen, Y. Han, M. Wang, Y. Yang, H. Chen, High photoconductive vertically oriented TiO₂ nanotube arrays and their composites with copper phthalocyanine, J. Phys. Chem. C 112 (2008) 2343-2348.

[55]    H. Xue, X. Kong, Z. Liu, C. Liu, J. Zhou, W. Chen, TiO₂ based metal-semiconductor-metal ultraviolet photodetectors, Appl. Phys. Lett. 90 (2007) 201118.

[56]    X. Kong, C. Liu, W. Dong, X. Zhang, C. Tao, L. Shen, J. Zhou, Y. Fei, S. Ruan Metal-semiconductor-metal TiO₂ ultraviolet detectors with Ni Electrodes, Appl. Phys. Lett. 94 (2009) 123502.

[57]    T. Tachikawa, T. Majima, Exploring the spatial distribution and transport behavior of charge carriers in a single titania nanowire, J. Am. Chem. Soc. 131 (2009) 8485-8495.

[58]    C. Fabrega, F. Hernandez-Ramırez, J. D. Prades, R. Jimenez-Dıaz, T. Andreu, J. R. Morante, On the photoconduction properties of low resistivity TiO₂ nanotubes, Nanotechnology 21 (2010) 445703.

[59]  R. S. Chen, C. A. Chen, H. Y. Tsai, W. C. Wang, Y. S. Huang, Ultrahigh efficient single-crystalline TiO$_2$ nanorod photoconductors, Appl. Phys. Lett. 100 (2012) 123108.

[60]  Y. Chang, C. Liu, Y. Tseng, C. Chen, C. Chen, H. Cheng, Direct probe of heterojunction effects upon photoconductive properties of TiO$_2$ nanotubes fabricated by atomic layer deposition, Nanotechnology 21 (2010) 225602.

[61]  Y. Han, C. Fan, G. Wu, H. Chen, M. Wang, Low-temperature solution processed utraviolet photodetector based on an ordered TiO$_2$ nanorod array_polymer hybrid, J. Phys. Chem. C 115 (2011) 13438-13445.

[62]  K.Zhu, T.B. Vinzant, N. R. Neale, and A.J. Frank, Removing structural disorder from oriented TiO$_2$ nanotube arrays: Reducing the dimensionality of transport and recombination in dye-sensitized solar cells, Nano Lett. 7 (2007) 3739-3746.

[63]  D. Kim, A. Ghicov, P. Schmuki, TiO$_2$ Nanotube arrays: Elimination of disordered top layers ("nanograss") for improved photoconversion efficiency in dye-sensitized solar cells, Electrochem. Commun. 10 (2008) 1835-1838.

[64]  G. Ali, S.H. Yoo, J.M. Kum, Y.N. Kim and S.O. Cho, A novel route to large-scale and robust free-standing TiO$_2$ nanotube membranes based on N$_2$ gas blowing combined with methanol wetting, Nanotechnology 22 (2011) 245602.

[65]  Y. Alivov, M. Pandikunta, S. Nikishin, Z Y Fan, The anodization voltage influence on the properties of TiO$_2$ nanotubes grown by electrochemical oxidation, Nanotechnology 20 (2009) 225602 (6pp).

[66]  K. Shankar, G.K. Mor, C.A. Grimes, Highly-ordered TiO$_2$ nanotube-arrays up to 220 μm in length: use in water photoelectrolysis and dye-sensitized solar cells, Nanotechnology 18 (2007) no.065707.

[67]  J.M. Macak, H. Hildebrand, U. Marten-Jahns, Mechanistic aspects and growth of large diameter self-organized TiO$_2$ nanotubes, J. Electroanal. Chem. 621 (2008) 254-266.

[68]  H. Yin, H. Liu, W. Z. Shen, The large diameter and fast growth of self-organized TiO$_2$ nanotube arrays achieved via electrochemical anodization, Nanotechnology 21 (2010) 035601(7pp).

[69]  S. Sreekantan, R. Hazan, Z. Lockman, Photoactivity of anatase-rutile TiO$_2$ nanotubes formed by anodization method, Thin solid films, 518 (2009) 16-21.

[70]    Y.L. Pang, A. Z. Abdullah, S. Bhatia, Effect of annealing temperature on the characteristics, sonocatalytic activity and reusability of nanotubes $TiO_2$ in the degradation of Rhodamine B, Appl. Catal. B: Environ. 100 (2010) 393-402.

[71]    D. Fang, Z. Luo, K. Huang, D. C. Lagoudas, Effect of heat treatment on morphology, crystalline structure and photocatalysis properties of $TiO_2$ nanotubes on Ti substrate and freestanding membrane, Applied Surface Science, 257 (2011) 6451-6461.

[72]    D.D. Li, P.C. Chang, C.J. Chien, J.G. Lu, Applications of tunable $TiO_2$ nanotubes as nanotemplate and photovoltaic device, Chem. Mater. 22 (2010) 5707-5711.

[73]    J.M. Macak, S. Albu, D.H. Kim, I. Paramasivam, S. Aldabergerova, P. Schmuki, Multilayer $TiO_2$-nanotube formation by two-step anodization, Electrochem. Solid-State Lett. 10 (2007) K28-K31.

[74]    K. Yasuda, P. Schmuki, Electrochemical formation of self-organized zirconium titanate nanotube multilayers,Electrochem. Commun. 9 (2007) 615-619.

[75]    B. Chen, K. Lu, Hierarchically Branched titania nanotubes with tailored diameters and branch numbers, Langmuir, 28 (2012) 2937-2943.

[76]    G. Butail, P. G. Ganesan, R. Teki, R. Mahima, N. Ravishankar, D. J. Duquette, G. Ramanath, Branched titania nanotubes through anodization voltage control, Thin Solid Films, 520(2011)235-238.

[77]    S.P. Albu, D. Kim, P. Schmuki, Growth of Aligned $TiO_2$ Bamboo-type nanotubes and highly ordered nanolace, Angew. Chem. Int. Ed. 47 (2008) 1916-1919.

[78]    A. Tighineanu, T. Ruff, S. Albu, R. Hahn, P. Schmuki, Conductivity of $TiO_2$ nanotubes: Influence of annealing time and temperature, Chemical Physics Letters 494 (2010) 260-263.

[79]    C.T. Yip, H. Huang, L. Zhou, K. Xie, Y. Wang , T. Feng , J. Li, W.Y. Tam, Direct and seamless coupling of $TiO_2$ nanotube photonic crystal to dye-sensitized solar cell: A single-step approach, Adv. Mater. 23(2011)5624-5268.

[80]    G.K. Mor, K. Shankar, M. Paulose, O.K. Varghese, C.A. Grimes, Use of highly-ordered $TiO_2$ nanotube arrays in dye-sensitized solar cells, Nano Lett., 6 (2006) 215-218.

[81]   O.K. Varghese, M. Paulose, C.A. Grimes, Long vertically aligned titania nanotubes on transparent conducting oxide for highly efficient solar cells, Nature nanotechnology 4 (2009) 592-597.

[82]   K. Zhu, N.R. Neale, A. F. Halverson, J.Y. Kim, A.J. Frank, Effects of annealing temperature on the charge-collection and light-harvesting properties of TiO$_2$ nanotube-based dye-sensitized solar cells, J. Phys. Chem. C 114(2010)13433-13441.

[83]   J. Yu, G. Dai, B. Cheng, Effect of crystallization methods on morphology and photocatalytic activity of anodized TiO$_2$ nanotube array films, J. Phys. Chem. C, 114(2010)19378-19385.

[84]   Z. Liu, J. Chen, Y. Zhang, L. Wu, X. Li, The effect of sandwiched Ag in the wall of TiO$_2$ nanotube on the photo-catalytic Performance, Materials Chemistry and Physics 128 (2011) 1-5.

[85]   X. Fang, Y. Bando, M. Liao, U.K. Gautam, C. Zhi, B. Dierre, B. Liu, T. Zhai, T. Sekiguchi, Y. Koide, D. Golberg, Single-crystalline ZnS nanobelts as ultraviolet-light sensors, Adv. Mater. 21 (2009) 2034-2039.

[86]   L. Hu, L.Wu, M. Liao, X. Fang, High-performance NiCo$_2$O$_4$ nanofilm photodetectors fabricated by an interfacial self-assembly strategy, Adv. Mater. 23 (2011) 1988-1992.

[87]   H. Yan , Z. Yu , K. Lu , Y. Zhang , Z. Wei, Self-assembly of graphenelike ZnO superstructured nanosheets and their application in hybrid photoconductors, Small 7 (2011) 3472-3478.

[88]   J.S. Jie, W.J. Zhang, Y. Jiang, X.M. Meng, Y.Q. Li, S.T. Lee, Photoconductive characteristics of single-crystal CdS nanoribbons, Nano Lett. 6 (2006) 1887-1892.

[89]   L. Li, X. Fang, T. Zhai, M. Liao, U.K. Gautam, X. Wu, Y. Koide, Y. Bando, D. Golberg, Electrical transport and high-performance photoconductivity in individual ZrS$_2$ nanobelts, Adv. Mater. 22 (2010) 4151-4156

[90]   Y. Cao, Z. Wei, S. Liu, L. Gan, X. Guo, W.Xu, M.L. Steigerwald, Z. Liu, D. Zhu, High-performance langmuir-blodgett monolayer transistors with high responsivity, Angew. Chem. 122 (2010) 6463-6467.

[91]   Y. Jin, J. Wang, B. Sun, J.C. Blakesley, N.C. Greenham, Solution-processed ultraviolet photodetectors based on colloidal ZnO nanoparticles, Nano Lett. 8 (2008) 1649-1653.

[92]    D. Xue, J. Wang, Y. Wang, S. Xin, Y. Guo, L. Wan, Facile synthesis of germanium nanocrystals and their application in organic-inorganic hybrid photodetectors, Adv. Mater. 23 (2011) 3704-3707.

[93]    G. Konstantatos, L. Levina, J. Tang, E.H. Sargent, Sensitive solution-processed $Bi_2S_3$ nanocrystalline photodetectors, Nano Lett. 8 (2008) 4002-4006.

[94]    J. Wang, Y. Wang, F. Cao, Y. Guo, L. Wan, Synthesis of monodispersed Wurtzite structure $CuInSe_2$ nanocrystals and their application in high-performance organic-inorganic hybrid photodetectors, J. Am. Chem. Soc. 132 (2010) 12218-12221.

[95]    C. Soci, A. Zhang, B. Xiang, S.A. Dayeh, D.P.R. Aplin, J. Park, X. Y. Bao, Y. H. Lo, and D. Wang, ZnO nanowire UV photodetectors with high internal gain, Nano Lett. 7 (2007) 1003-1009.

[96]    B. Chitara, L.S. Panchakarla, S.B. Krupanidhi, C.N.R. Rao, Infrared Photodetectors Based on Reduced Graphene oxide and graphene nanoribbons, Adv. Mater. 23 (2011) 5419-5424.

[97]    M. Liao, X. Wang, T. Teraji, S. Koizumi, Y. Koide, Light intensity dependence of photocurrent gain in single-crystal diamond detectors, Phys. Rev. B 81 (2010) 033304.

[98]    M. Chen , L. Hu , J. Xu , M. Liao, L. Wu, X. Fang, ZnO hollow-sphere nanofilm-based high-performance and low-cost photodetector, Small 7 (2011) 2449-2453.

[99]    T. Zhai, L. Li , X.Wang, X. Fang, Y. Bando, D. Golberg, Recent developments in one-dimensional inorganic nanostructures for photodetectors, Adv. Funct. Mater. 20 (2010) 4233-4248.

[100]  C. Richter, C.A. Schmuttenmaer, Exciton-like trap states limit electron mobility in $TiO_2$ nanotubes, Nat. Nanotechnol. 5 (2010) 769-772.

[101]  F. Xia, T. Mueller, Y. Lin, A. Valdes-Garcia, P. Avouris, Ultrafast graphene photodetector, Nat. Nanotechnol. 4 (2009) 839-843.

[102]  M. Afsal, C.Wang, L. Chu, H. Ouyang, L. Chen, Highly sensitive metal-insulator-semiconductor UV photodetectors based on $ZnO/SiO_2$ core-shell nanowires, J. Mater. Chem. 22 (2012) 8420-8425.

[103]  Z. Lockman, S. Sreekantan, S. Ismail, L. Schmidt-Mende, J.L. MacManus-Driscoll, Influence of anodisation voltage on the dimension of titania nanotubes, J. Alloys Compd. 503 (2010) 359-364.

[104]  F. Wang, Y. Liu, W. Dong, M. Shen, Z. Kang, Tuning $TiO_2$ Photoelectrochemical properties by nanoring/nanotube combined structure, J. Phys. Chem. C 115 (2011) 14635-14640.

[105]  S. Bauer, A. Pittrof, H.Tsuchiya, P. Schmuki, Size-effects in $TiO_2$ nanotubes: Diameter dependent anatase / rutile stabilization, Electrochem Commun. 13 (2011) 538-541.

[106]  R. Calarco, M. Marso, T. Richter, A. Aykanat, R. Meijers, A. Hart, T. Stoica, H. Luth, Size-dependent Photoconductivity in MBE-Grown GaN-Nanowires, Nano Lett. 5 (2005) 981-984.

[107]  H. Chen, R. Chen, F. Chang,L. Chen, K. Chen, Y. Yang, Size-dependent photoconductivity and dark conductivity of m-axial GaN nanowires with small critical diameter, Appl. Phys. Lett. 95 (2009) 143123.

[108]  K. Zhu, T.B. Vinzant, N.R. Neale, A.J. Frank, Enhanced charge-collection efficiencies and light scattering in dye-sensitized solar cells using oriented $TiO_2$ nanotubes arrays, Nano Lett. 7 (2007) 69-74.

[109]  N. Liu, K. Lee, P. Schmuki, Small diameter $TiO_2$ nanotubes vs. nanopores in dye sensitized solar cells, Electrochem Commun.15 (2012) 1-4.